

Exploring the Relationship Between Stellar Mass, Metallicity, and Star Formation Rate at $z \sim 2.3$ in KBSS-MOSFIRE

NATHALIE A. KORHONEN CUESTAS ^{1,2} ALLISON L. STROM ^{1,2} TIM B. MILLER ² CHARLES C. STEIDEL ³
RYAN F. TRAINOR ⁴ GWEN C. RUDIE ⁵ AND EVAN HAZE NUÑEZ ³

¹*Department of Physics and Astronomy, Northwestern University, 2145 Sheridan Road, Evanston, IL 60208, USA*

²*Center for Interdisciplinary Exploration and Research in Astrophysics (CIERA), Northwestern University, 1800 Sherman Avenue, Evanston, IL 60201, USA*

³*Cahill Center for Astronomy and Astrophysics, California Institute of Technology, MS 249-17, Pasadena, CA 91125, USA*

⁴*Department of Physics and Astronomy, Franklin & Marshall College, 637 College Avenue, Lancaster, PA 17603, USA*

⁵*The Observatories of the Carnegie Institution for Sciences, 813 Santa Barbara Street, Pasadena, CA 91101, USA*

ABSTRACT

The metal enrichment of a galaxy is determined by the cycle of baryons in outflows, inflows, and star formation. The relative contribution and timescale of each process sets the relationship between stellar mass, metallicity, and the star formation rate (SFR). In the local universe, galaxies evolve in an equilibrium state where the timescales on which SFR and metallicity vary are comparable, and they define a surface in mass-metallicity-SFR space known as the Fundamental Metallicity Relation (FMR). However, high-redshift observations suggest that this state of equilibrium may not persist throughout cosmic time. Using galaxies from the Keck Baryonic Structure Survey (KBSS) observed with MOSFIRE, we explore the relationship between stellar mass, gas-phase oxygen abundance, and SFR at $z \sim 2.3$. Across multiple strong-line calibrations and SFR calculation methods, KBSS galaxies are inconsistent with the locally-defined FMR. We use both parametric and non-parametric methods of exploring a mass-metallicity-SFR relation. When using a parametric approach, we find no significant reduction mass-metallicity relation scatter when folding in SFR as a third parameter, although a non-parametric approach reveals that there could be a weak, redshift-dependent anticorrelation between residual gas-phase oxygen abundance and SFR. Injection-recovery tests show that a significant reduction in scatter requires a stronger anticorrelation between SFR and residual metallicity. Our results suggest that the local FMR may not persist to $z \sim 2.3$, implying that $z \sim 2.3$ galaxies at this redshift may not be in the equilibrium state described by the FMR and are more similar to higher redshift galaxies.

1. INTRODUCTION

The flow of gas into and out of a galaxy sets its evolutionary trajectory. Metal-poor gas can be accreted from the circumgalactic medium or through interactions with nearby lower-mass galaxies, creating a gas-rich, metal-poor environment and triggering episodes of star formation. Eventually, these same stars will enrich the interstellar medium (ISM) through stellar winds and supernova explosions. Galactic winds driven by supernovae, massive stars, and active galactic nuclei (AGN) can transport gas out of the galaxy, depleting the gas reservoir, curtailing star formation, and transporting

metals out of the galaxy. Understanding how these processes influence the galactic ecosystem and change over cosmic time is necessary to gain a full picture of galaxy growth and evolution.

Elemental abundances are sensitive to the relative contributions of metal-poor inflows, gas-rich outflows, and star formation. As a result, chemical scaling relations are a key probe of the baryon cycle. Lequeux et al. (1979) first identified a correlation between the luminosity, mass, and metallicity of H II regions in irregular and blue compact galaxies. A similar luminosity-metallicity relation was observed by Garnett (2002) in irregular galaxies and by Pilyugin et al. (2004) in spiral galaxies. Using a sample of $\sim 53,000$ Sloan Digital Sky Survey (SDSS; York et al. 2000) galaxy spectra, Tremonti et al. (2004) robustly characterized the mass-metallicity rela-

tion (MZR). Tremonti et al. (2004) found that lower-mass galaxies are more metal-poor than higher-mass galaxies, and the slope of the relationship becomes shallower at higher masses. The slope of the MZR can only be reproduced by models that consider outflows and inflows (Kobayashi et al. 2007; Finlator & Davé 2008; Davé et al. 2017), demonstrating that galaxies do not evolve as “closed-box” systems (Tremonti et al. 2004; Finlator & Davé 2008).

Since the analysis by Tremonti et al. (2004), the MZR has been observed at a range of redshifts ($z \lesssim 1$: Savaglio et al. 2005; Liu et al. 2008; Cowie & Barger 2008; Pérez-Montero et al. 2009, $z \sim 2$: Erb et al. 2006; Panter et al. 2008; Mannucci et al. 2009; Steidel et al. 2014; Sanders et al. 2018; Strom et al. 2022, and $z \gtrsim 3$: Maiolino et al. 2008; Troncoso et al. 2014; Onodera et al. 2016; Sanders et al. 2021; Curti et al. 2023; Nakajima et al. 2023, among many others). The MZR evolves towards lower normalizations at higher redshifts, meaning that at a fixed stellar mass, galaxies are more metal-poor at higher redshifts. A variety of processes could drive the MZR’s evolution towards lower metallicities. Higher gas fractions, stronger outflows due to either enhanced star formation or AGN activity, and higher inflow rates of metal-poor gas at higher redshifts could all lead to the observed redshift evolution (e.g., Savaglio et al. 2005; Erb et al. 2006; Maiolino et al. 2008; Mannucci et al. 2009).

The dispersion of galaxies about the MZR (~ 0.1 dex in the Tremonti et al. 2004 sample) has also been extensively studied. Offsets relative to the MZR have been correlated with star formation rate (SFR), specific star formation rate (sSFR), gas mass, galaxy size, and galaxy color (Tremonti et al. 2004; Ellison et al. 2008; Mannucci et al. 2010; Salim et al. 2014; Bothwell et al. 2016). For local galaxies at fixed mass, metallicity is inversely correlated with SFR, leading both Lara-López et al. (2010) and Mannucci et al. (2010) to suggest the presence of a more fundamental, three-parameter relationship linking stellar mass (M_*), gas-phase metallicity (Z_g), and SFR that underpins the MZR and can reproduce both the MZR’s observed scatter and its redshift evolution. Mannucci et al. (2010) specifically defined a three-dimensional surface in M_* - Z_g -SFR space, which local galaxies populate with very little scatter (~ 0.05 dex for SDSS galaxies). Importantly, this Fundamental Metallicity Relation (FMR) was hypothesized to be redshift-invariant, implying a mechanism for galaxy growth and enrichment that is also redshift invariant.

The FMR is consistent with the gas-regulator model described by Lilly et al. (2013), assuming constant star formation efficiency and outflow mass loading factors.

In this model, galaxies are continuously fed by a slowly-evolving infall of gas, the SFR is instantaneously regulated by the gas mass of the galaxy, and mass loss rates scale with SFR, thereby resulting a redshift-invariant FMR.

The presence (or absence) of the FMR at high redshift has been widely investigated (e.g., Troncoso et al. 2014; Zahid et al. 2014; Maier et al. 2015; Yabe et al. 2015; Kacprzak et al. 2016; Onodera et al. 2016; Sanders et al. 2021), and the James Webb Space Telescope (JWST) has allowed FMR studies to push to ever higher redshifts (e.g., Curti et al. 2023; Nakajima et al. 2023; Curti et al. 2024). However, these works vary significantly in the methods used to measure oxygen abundance and assess consistency with the local FMR. Oxygen abundance is often estimated using strong-line calibrations (e.g., Steidel et al. 2014; Zahid et al. 2014; Wuyts et al. 2016; Kashino et al. 2017; Curti et al. 2024), although sometimes direct measurements via the T_e method are accessible, either in individual spectra (Calabrò et al. 2017; Curti et al. 2023; Nakajima et al. 2023; Revalski et al. 2024) or in composite spectra (Sanders et al. 2021; Topping et al. 2021). Photoionization models are also sometimes used (Maier et al. 2014; Calabrò et al. 2017). Galaxies may also be treated individually (Curti et al. 2023) or binned by mass, SFR, or redshift (e.g., Sanders et al. 2015; Yabe et al. 2015; Sanders et al. 2018).

The FMR and more general M_* - Z_g -SFR relationships are probed in three main ways: using a similar methodology to Mannucci et al. (2010) to find the projection of least scatter (e.g., Andrews & Martini 2013; Onodera et al. 2016; Sanders et al. 2021), direct comparison to a locally-defined FMR (e.g., Maier et al. 2014; Sanders et al. 2015; Yabe et al. 2015; Curti et al. 2023, 2024), or by quantifying the correlation between residual metallicity (defined relative to the median for galaxies of the same mass) and SFR (e.g., Salim et al. 2014; Zahid et al. 2014; Wuyts et al. 2016).

Given the broad range of possible approaches, consensus remains elusive. Some find high-redshift galaxies to be consistent with a locally-calibrated FMR plane (Maier et al. 2015; Yabe et al. 2015; Kacprzak et al. 2016; Topping et al. 2021), supporting the existence of a redshift-invariant FMR, while others observe a M_* -SFR- Z_g relationship but find their galaxies to be offset from local FMR planes (Zahid et al. 2014; Salim et al. 2015; Kashino et al. 2017; Sanders et al. 2018), instead suggesting that the FMR evolves with redshift. Still others find no evidence of the FMR *or* a three parameter correlation (Steidel et al. 2014; Wuyts et al. 2016).

This paper aims to characterize the relationship between stellar mass, gas-phase oxygen abundance, and

SFR at $\langle z \rangle = 2.29$ using a large, homogeneously selected sample of galaxies from the complete Keck Baryonic Structure Survey (KBSS) and determine the extent to which the data are consistent with the locally-defined FMR. By employing different analysis methods we also aim to explore how our results, and the results of other studies, depend on which method is used to define and characterize the FMR. For the sake of clarity, we will use FMR to specifically refer to a redshift-invariant surface in M_* - Z_g -SFR space, as proposed by Mannucci et al. (2010). Any other correlations between M_* , Z_g , and SFR will be referred to as a M_* - Z_g -SFR relationship. The galaxy sample and measured properties are introduced in Section 2. The star forming main sequence (SFMS) and MZR for KBSS galaxies are reported in Sections 3.1 and 3.2. In Section 3.4 we compare KBSS galaxies to the locally-defined FMR, and in Sections 3.3 and 3.5, we explore parametric and non-parametric approaches. In Section 4 we attempt to reconcile the results of both parametric and non-parametric methods (Section 4.1), compare our results to both local and high- z surveys (Section 4.2), and discuss potential physical implications (Section 4.3). Lastly, we present our conclusions in Section 5.

Throughout this paper, we assume a Λ CDM cosmology with $H_0 = 70 \text{ km s}^{-1} \text{ Mpc}^{-1}$, $\Omega_\Lambda = 0.7$, and $\Omega_m = 0.3$ and adopt the Solar oxygen abundance value reported in Asplund et al. (2009), $12 + \log(\text{O}/\text{H})_\odot = 8.69$, but assume $Z_\odot = 0.02$ as this is the value adopted by BPASS. Individual emission lines are referred to using their vacuum wavelength in Angstroms.

2. THE KECK BARYONIC STRUCTURE SURVEY

The galaxies analyzed in this paper were observed as part of the Keck Baryonic Structure Survey (KBSS; Rudie et al. 2012; Steidel et al. 2014). KBSS is a targeted spectroscopic survey designed to observe galaxies at $z \sim 1.5 - 3.5$ (see Figure 1 for the redshift distribution of galaxies analyzed in this paper) in fifteen quasar fields over a total area of $\sim 0.24 \text{ deg}^2$, with substantial rest-UV and rest-optical imaging and spectroscopy conducted using the Keck LRIS (Oke et al. 1995) and MOSFIRE (McLean et al. 2012) instruments. Here, we only consider galaxies with rest-optical spectra, which make up the KBSS-MOSFIRE subsample. Importantly, the strong rest-optical lines produced in H II regions are redshifted into the NIR J , H , and K bands at $1.9 < z < 2.7$, with a subset of these strong lines accessible at $z \sim 1.5$ and $z \sim 3$. Most KBSS galaxies were selected based on their rest-UV colors (for further detail, see Adelberger et al. 2004; Steidel et al. 2004). Some additional objects are selected based on their \mathcal{R} - K colors in order to

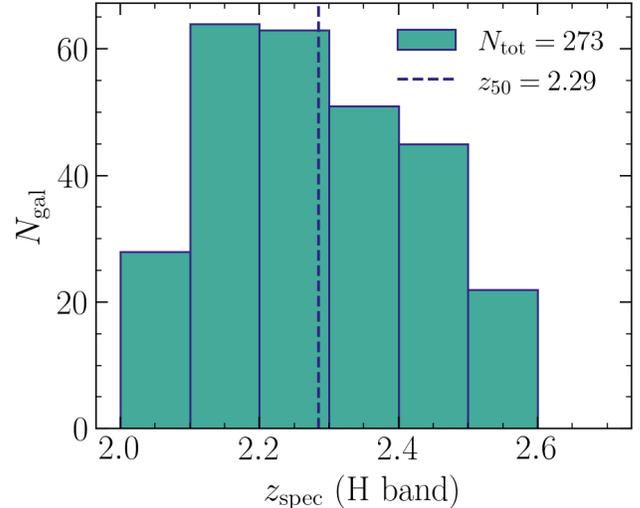


Figure 1. The redshift distribution of the O3N2-selected KBSS galaxies. The sample probes a redshift range of $2.0 < z < 2.6$, with a median $z_{50} = 2.29$.

mitigate a slight preference towards highly star-forming galaxies (Strom et al. 2017).

For further detail on the KBSS survey design, photometric data, spectroscopy, and data reduction, see Steidel et al. (2004); Reddy et al. (2012); Steidel et al. (2014) and Strom et al. (2017). Here, we discuss some of the more pertinent aspects of KBSS-MOSFIRE.

2.1. Stellar Mass

To estimate the stellar mass (M_*) of each galaxy and obtain object-by-object posteriors, we use the spectral energy distribution (SED)-fitting code BAGPIPES (Carnall et al. 2018) and broadband photometry. All fifteen KBSS quasar fields are observed in at least eight photometric bands including the optical U_n , G , and \mathcal{R} s bands, near-IR J and K_s , and mid-IR IRAC Ch1 and 2. Fourteen fields have photometry in WFC3 F140W and F160W (Q1549 lacks F140W coverage and Q0821 lacks F160W coverage). Nine of the fields are also observed in the near-IR H band with Magellan/FourStar and six fields are observed in IRAC Ch 3. Photometry in B band, WFC3 F110W, F125W, and F814W is also available for select fields. For further detail on the photometry in KBSS fields, see Theios et al. (2019). The photometry has also been corrected for the contribution from emission lines.

The BAGPIPES model galaxy spectra use BPASS (v2.2.1 Stanway & Eldridge 2018) binary stellar population models with a Kroupa (2001)-like IMF with an upper mass slope of -2.35 and a maximum stellar mass of $100M_\odot$. We do, however, rescale the resulting stellar masses to a Chabrier (2003) IMF to allow for closer

comparison to other samples. The nebular continuum is modeled using CLOUDY (Ferland et al. 2017), where the input spectrum is taken from the BPASS grids (Carnall et al. 2018). Notably, we do not consider the effect of nebular emission lines on the model galaxy SED, since the photometry has already been corrected for the contribution of emission lines. We adopt the SMC (Gordon et al. 2003) dust reddening curve, which Theios et al. (2019) found to yield the best agreement between $H\alpha$ -based SFRs and SED-based SFRs when applied to the stellar continuum of KBSS galaxies. We limit the metallicity range to $[0, 0.5]Z_{\odot}$, assuming the same value for both the stellar and gas-phase metallicities; the log of the ionisation parameter (defined as the ratio between ionizing photon density and hydrogen number density $U \equiv n_{\gamma,i}/n_H$) range to $[-3.5, -2.5]$; the dust attenuation A_V range to $[0, 2]$ magnitudes; and the log of the stellar mass range to $[0, 15]$. The redshift of a galaxy was held fixed at the spectroscopic redshift.

We implement a non-parametric, continuity star formation history (SFH), which has been shown to more accurately recover galaxy properties and their associated uncertainties and introduce less bias than a parametric star formation history (Carnall et al. 2019; Leja et al. 2019). To fit the SFH, BAGPIPES fits the change in SFR ($\Delta \log(\text{SFR})$) between set time bins. We set the bins to be 0, 10, 100, 250, 500, 1000, 1500, 2000, 2500, 3000, and 3500 Myr before the time of observation. In practice, the oldest time bin is sometimes not considered as it is excluded by the galaxy’s spectroscopic redshift. The prior on $\Delta \log(\text{SFR})$ is set as a Student’s-t distribution with a mean value of 0, a scale factor of 0.3, and 2 degrees of freedom, as in Leja et al. (2019), which has a preference towards smaller changes in SFR between time bins, resulting in generally smoother SFHs.

The results of our SED-fitting are broadly consistent with previously published KBSS stellar masses (Theios et al. 2019). The primary difference is the adoption of a non-parametric SFH; previously, a constant SFH had been assumed. A non-parametric SFH tends to produce slightly higher M_{\star} estimates as it allows for a more extended SFH, during which galaxies build up more mass. The difference is small (~ 0.06 dex, or a 14% increase in M_{\star}): the median stellar mass assuming a constant SFH is $M_{\star} \sim 5.6 \times 10^9 M_{\odot}$ and the median stellar mass assuming a non-parametric SFH is $M_{\star} \sim 6.4 \times 10^9 M_{\odot}$. Further comparison between the stellar masses used here and the stellar masses reported in Theios et al. (2019) will be discussed in Strom et al. (in prep).

2.2. Strong Line Measurements and Dust Correction

Emission line measurements were made from the extracted 1D MOSFIRE spectra (Steidel et al. 2014). The continuum is estimated using stellar population synthesis models from Bruzual & Charlot (2003) fit to the observed galaxy SED, which self-consistently account for the effects of dust extinction and stellar Balmer absorption features (for further detail see Strom et al. 2017). Strong lines in a single MOSFIRE band are fit using Gaussians with a single redshift and line width. The flux ratios of the $[\text{O III}]\lambda\lambda 4959, 5008$ and $[\text{N II}]\lambda\lambda 6549, 6585$ doublets were fixed at 1:3, as set by atomic physics (Storey & Zeippen 2000). Line fluxes were corrected for potential slit losses using the method detailed in Strom et al. (2017). In the case of some higher- z galaxies, $[\text{O III}]\lambda 5007$ falls outside of H band, and so cannot be directly measured in the spectrum. In these cases, we used the detection of $[\text{O III}]\lambda 4959$ to estimate the flux of $[\text{O III}]\lambda 5007$ using the same 1:3 flux ratio.

To account for the effect of dust attenuation toward star-forming regions, we adopt a Milky Way dust extinction curve with $R_V = 3.1$ (Cardelli et al. 1989), consistent with previous KBSS studies (Theios et al. 2019). Extinction is estimated using the Balmer decrement, assuming a theoretical value of $H\alpha/H\beta = 2.86$ (Case B; Osterbrock 1989). We imposed a selection criterion that the SNR of $H\alpha/H\beta > 5$. Given that the uncertainty of extinction corrections scale as $\sim (H\alpha/H\beta)^{k_{\lambda}}$, where k_{λ} is the value of the reddening curve at a specific wavelength (for reference, $k_{H\alpha} = 2.53$), small uncertainties in the Balmer decrement can propagate as large uncertainties in the corrected line flux. In cases where the Balmer decrement was found to be < 2.86 , zero extinction was assumed. Dust-corrected line fluxes were only used in SFR calculations and not in the calculation of strong-line ratios. The strong-line ratios used to infer oxygen abundance in this paper require emission lines that are fairly close to each other in wavelength, meaning that the ratio is only weakly affected by dust attenuation and a reddening correction is not necessary.

2.3. Gas-Phase Oxygen Abundance

The most accurate measurements of gas-phase oxygen abundances require an electron temperature (T_e) measurement. The auroral emission lines needed measure T_e are intrinsically much fainter than strong nebular emission lines. For example, the auroral line $[\text{O III}]\lambda 4363$ can be $\sim 100\times$ fainter than the strong nebular line $[\text{O III}]\lambda 5007$, making them difficult to detect at high redshift (although this is changing in the era of JWST, see for example Schaerer et al. 2022; Curti et al. 2023; Hsiao et al. 2024; Rogers et al. 2024). Alternatively, we can use strong-line calibrations, which correlate the ratio of

strong rest-optical nebular emission lines with oxygen abundance. The calibration can be based on samples with direct T_e measurements (e.g., [Marino et al. 2013](#); [Bian et al. 2018](#)), photoionization modeling (e.g., [McGaugh 1991](#); [Strom et al. 2018](#)), or on a combination of the two (e.g., [Pettini & Pagel 2004](#)).

There are several limitations to the use of strong-line calibrations. Many calibrations are based on low- z galaxies, with systematically different ISM abundances and ionizing radiation ([Masters et al. 2014](#); [Steidel et al. 2014](#); [Shapley et al. 2015](#); [Strom et al. 2017](#); [Shapley et al. 2024](#)), meaning that applying local calibrations at high redshift can introduce bias. Using calibrations based on H II regions or low-redshift analogues to high-redshift galaxies can go some way to addressing this issue, as the calibration sample may reflect ISM conditions more similar to those in high-redshift galaxies. Improved observational capabilities due to JWST has also allowed ongoing work to recalibrate these strong-line calibrations *in-situ* by directly observing auroral lines at ever higher redshifts ([Laseter et al. 2024](#); [Sanders et al. 2024](#); [Scholte et al. 2025](#)).

However, strong-line ratios are used throughout the literature to produce MZR (e.g., [Savaglio et al. 2005](#); [Erb et al. 2006](#); [Revalski et al. 2024](#); [Curti et al. 2024](#)) and establish the existence of the FMR (e.g., [Mannucci et al. 2010](#); [Maier et al. 2015](#); [Curti et al. 2020](#)), so with their limitations in mind, we apply strong-line calibrations to KBSS galaxies to facilitate comparison with previous work. We test two different strong-line ratios, O3N2 and N2, which we define as

$$\text{O3N2} \equiv \log\left(\frac{[\text{O III}]\lambda 5008}{\text{H}\beta}\right) - \log\left(\frac{[\text{N II}]\lambda 6585}{\text{H}\alpha}\right) \quad (1)$$

$$\text{N2} \equiv \log\left(\frac{[\text{N II}]\lambda 6585}{\text{H}\alpha}\right) \quad (2)$$

O3N2 and N2 are both sensitive to ionization parameter as well as oxygen abundance ([Kewley & Dopita 2002](#)), introducing significant systematic uncertainty to individual oxygen abundance measurements. Another widely-used strong-line indicator of oxygen abundance is R23 $\equiv \log\left(\frac{([\text{O III}]\lambda\lambda 4960, 5008 + [\text{O II}]\lambda\lambda 3727, 3729)/\text{H}\beta}{\text{H}\alpha}\right)$, which is less sensitive to ionization parameter than O3N2 and N2. Additionally, the R23 ratio can be modified by weighing $[\text{O III}]\lambda\lambda 4960, 5008$ and $[\text{O II}]\lambda\lambda 3727, 3729$ such that the dependence on ionization parameter is minimized ([Laseter et al. 2024](#); [Scholte et al. 2025](#)). However, R23 is double-valued and sensitive to stellar iron abundance at its turning point (e.g., [Strom et al. 2018](#)). Since many KBSS galaxies lie near the turning point and some lie

beyond the range of R23 allowed by most strong-line calibrations, R23-based oxygen abundances are not investigated in detail here. However, it is worth noting that we have conducted our analysis using galaxies with reliably-measured R23 and the R23 calibration from [Strom et al. \(2018\)](#) and find the same qualitative results as what is reported in this paper.

For each line ratio, we test four different strong-line calibrations. Each calibration differs in terms of the parent sample and method used to measure abundance. Moreover, each calibration produces an MZR with a different slope, normalization, and intrinsic scatter. Comparing different calibrations therefore allows us to test whether the detection of the FMR differs depending on the associated MZR slope, MZR scatter, or chosen strong-line ratio.

The calibrations all take the form

$$12 + \log(\text{O}/\text{H}) = A - B \times \text{R} \quad (3)$$

Where R is the line ratio, and A and B are constants unique to the specific calibration. For a summary of the different calibrations we use, see [Table 1](#). The [Pettini & Pagel \(2004, hereafter PP04\)](#) calibration is based on observations of extragalactic H II regions where either T_e could be directly measured or the spectrum could be robustly reproduced by photoionization models. The calibration has been applied to different samples at comparable redshifts to KBSS (e.g., [Topping et al. 2021](#)), allowing for a direct comparison between our results. [Steidel et al. \(2014, hereafter S14\)](#) use the same observations as PP04, but base the calibration only on H II regions where oxygen abundance was measured via the T_e method and the value of N2 was within the range observed in KBSS-MOSFIRE galaxies. [Marino et al. \(2013, hereafter M13\)](#) also use T_e measurements of H II regions, which were observed in the CALIFA survey ([Sánchez et al. 2012, 2013](#)). The direct metallicity measurement is combined with the metallicity estimated from strong nebular oxygen, nitrogen, and sulfur emission lines, as described in [Pilyugin et al. \(2010\)](#) with the goal of producing a more accurate overall calibration. The remaining calibrations are all based on observations of galaxies rather than H II regions. [Bian et al. \(2018, hereafter B18\)](#) identify low-redshift galaxies that lie on the $z \sim 2$ star forming sequence in the N2-BPT diagram as potential analogs to high-redshift galaxies. The calibration is based on direct measurements of T_e in these galaxies. Lastly, the calibrations from [Strom et al. \(2018, hereafter S18\)](#) are based on 150 KBSS galaxies where the abundance was estimated using photoionization models. Therefore, we are able to compare calibrations which use T_e measurements, pho-

Table 1. Summary of the eight different line ratios used in this paper. A and B refer to the constants in Equation 3.

Calibration	Line Ratio	A	B
Pettini & Pagel (2004)	O3N2	8.73	0.32
Marino et al. (2013)	O3N2	8.533	0.214
Bian et al. (2018)	O3N2	8.97	0.39
Strom et al. (2018)	O3N2	8.75	0.21
Marino et al. (2013)	N2	8.743	-0.462
Steidel et al. (2014)	N2	8.62	-0.36
Bian et al. (2018)	N2	8.82	-0.49
Strom et al. (2018)	N2	8.77	-0.34

toionization models, or a combination and are based on populations of local H II regions, local analogues to high- z galaxies, and $z \sim 2.3$ galaxies.

To ensure that the necessary lines are well-measured, we select galaxies where the SNR of all emission lines used in a given strong-line calibration is > 3 and the SNR of $H\alpha/H\beta > 5$. This criteria results in a sample of 273 galaxies with well-measured O3N2 and 274 galaxies with well-measured N2.

2.4. Star-Formation Rate

SFR can be estimated as part of the SED fitting, but due to the degeneracy with fit parameters such as age and stellar mass, we prefer SFR estimates derived from the $H\alpha$ luminosity ($\mathcal{L}_{H\alpha}$). $\mathcal{L}_{H\alpha}$ must be multiplied by a conversion factor to determine SFR (e.g., Kennicutt & Evans 2012, hereafter KE12). However, the conversion factor is typically based on local stellar populations and ISM conditions, and may not be reflective of the ionizing photon production at high redshift. Galaxies at higher redshifts have systematically lower gas-phase metallicities, meaning that young, massive stars that produce much of the Lyman continuum are also more metal-poor. Metal-poor stars produce more ionizing photons per unit mass than metal-rich stars, and as a result, there are more photons available for absorption and re-emission in the ISM. Therefore, a smaller number of metal-poor stars can produce the same $\mathcal{L}_{H\alpha}$ as a larger population of more metal-rich stars (Zhang et al. 2013). Due to the comparatively low contribution of Type Ia supernova enrichment, the abundance *patterns* in high- z galaxies also differ significantly from solar: high- z galaxies tend to show an enhanced α -element abundance compared to the iron abundance (Kobayashi et al. 2020). Consequently, high- z galaxies with sub-solar gas-phase oxygen abundances will have even more sub-solar $[\text{Fe}/\text{H}]$. Assuming that $[\text{Fe}/\text{H}]$ traces stellar metallicity, this corresponds to $Z_*/Z_\odot \sim 0.1$ for $z \sim 2 - 3$ galaxies (Steidel

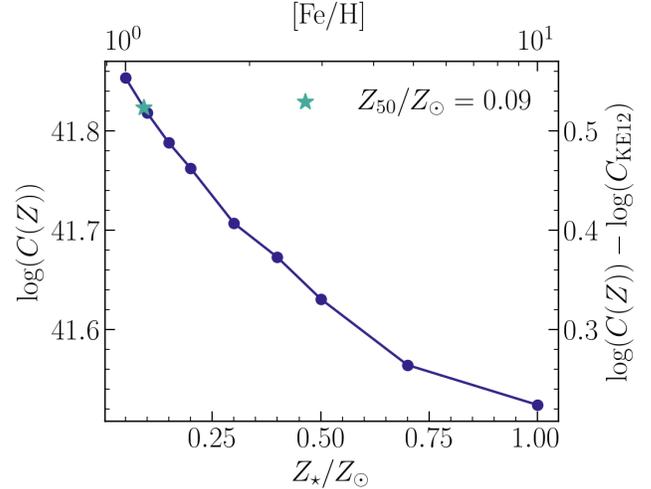


Figure 2. $\mathcal{L}_{H\alpha}$ to SFR conversion factor vs. stellar metallicity. Values calculated from BPASS models are shown in purple, and the median stellar metallicity in the KBSS sample ($Z_{50}/Z_\odot = 0.09$) is shown by the teal star. Adopting $\log(C(Z_*))$ results in a lower SFR than what is predicted by KE12 since $\log(C(Z_*))$ remains larger than $\log(C_{\text{KE12}}) = 41.30$ at all $Z_* \leq Z_\odot$, and the discrepancy is larger for more metal-poor galaxies.

et al. 2016; Strom et al. 2018; Topping et al. 2020). Neglecting the relationship between metallicity and ionizing photon production can lead to an overestimation of the SFR at high redshift.

To capture the impact of metallicity on the ionizing spectrum, we adopt a metallicity-dependent conversion factor between $\mathcal{L}_{H\alpha}$ and SFR. This relationship takes the form

$$\log(\text{SFR}) = \log(\mathcal{L}_{H\alpha}) - \log(C(Z_*)) \quad (4)$$

Where $\mathcal{L}_{H\alpha}$ is the $H\alpha$ luminosity in erg s^{-1} , SFR is given in $M_\odot \text{yr}^{-1}$, and $C(Z_*)$ is the metallicity-dependent conversion factor. $C(Z_*)$ is calculated using model SEDs at different stellar metallicities produced using BPASS (v2.2.1 Stanway & Eldridge 2018), assuming a constant SFH over 100 Myr, a Chabrier (2003) IMF with a maximum stellar mass of $100 M_\odot$, and including the effects of binary stars. Using f_λ from the BPASS SED, we integrate up to 912 \AA to calculate the ionizing photon production:

$$N(H^0) = \int_0^{912 \text{ \AA}} \frac{\lambda f_\lambda}{hc} d\lambda \quad (5)$$

Then, using Equation 9 in Leitherer & Heckman (1995), we calculate $\mathcal{L}_{H\alpha}$ per $M_\odot \text{yr}^{-1}$ of star formation:

$$\mathcal{L}_{H\alpha} [\text{erg s}^{-1}] = 1.36 \times 10^{-12} N(H^0) [\text{s}^{-1}] \quad (6)$$

Table 2. Metallicity-dependent H α luminosity to SFR conversion factors after 100 Myr of constant star formation.

Z_*	$\log(C(Z_*))$
0.001	41.680
0.002	41.647
0.003	41.619
0.004	41.595
0.006	41.544
0.008	41.512
0.010	41.473
0.014	41.411
0.020	41.373

The resulting conversion factors are listed in Table 2 and are shown in Figure 2, which highlights the importance of considering the effect of metallicity. $C(Z_*)$ decreases monotonically with Z_* and is higher than the KE12 conversion factor, rescaled to a Chabrier (2003) IMF, at solar metallicity ($\log(C_{\text{KE12}}) = 41.30$). At the median metallicity of KBSS galaxies in the O3N2 sample ($Z_{50} = 0.09Z_{\odot}$, teal star in Figure 2), the KE12 conversion factor is 0.35 dex lower than the BPASS conversion factor, leading to a 0.35 dex overestimation of $\log(\text{SFR})$.

For each galaxy we adopt a stellar metallicity based on that galaxy’s inferred iron abundance, which is determined from their oxygen abundance and assuming the oxygen and iron MZR have the same slope, but different normalizations (Cullen et al. 2019; Sanders et al. 2020; Topping et al. 2020; Strom et al. 2022; Stanton et al. 2024). We adopt a constant offset for all galaxies of $[\text{O}/\text{Fe}] = 0.35$ (Strom et al. 2022) and infer $[\text{Fe}/\text{H}]$ according to

$$[\text{Fe}/\text{H}] = \log(\text{O}/\text{H}) - \log(\text{O}/\text{H})_{\odot} - 0.35 \quad (7)$$

The effect of adopting a metallicity-dependent conversion factor is twofold. The first order effect is a systematic shift towards a lower SFR. This effect arises from the fact that $\log(C(Z_*)) > \log(C_{\text{KE12}})$ at all $Z_* < Z_{\odot}$ (see Figure 2). The median Z_* -dependent SFR, using the PP04 calibration ($\text{SFR}(Z)_{\text{PP04}}^{\text{O3N2}}$) is $9.3M_{\odot}\text{yr}^{-1}$, while the median SFR estimated by the KE12 (SFR_{KE12}) relation is $30.9M_{\odot}\text{yr}^{-1}$ for galaxies in the O3N2 sample, reflecting the systematic shift towards lower SFR. It should be noted that this bulk shift is not specifically due to the metallicity dependence in the conversion factor: adopting a single conversion factor (e.g., $\log(C) = 41.67$ as in Shapley et al. 2023) that better reflects the photon production of metal-poor stars can create the same effect. The second order effect can be clearly seen in Figure 3: more metal-poor galaxies have a larger discrepancy between SFR_{KE12} and $\text{SFR}(Z)$. The magnitude of

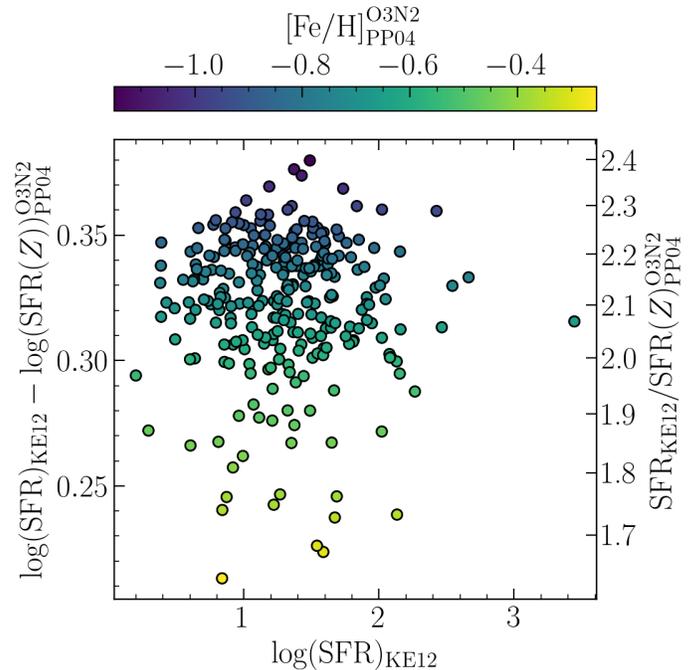


Figure 3. Difference between $\log(\text{SFR}_{\text{KE12}})$ and $\log(\text{SFR}(Z))$ vs. $\log(\text{SFR}_{\text{KE12}})$, colour-coded by $[\text{Fe}/\text{H}]$ for the KBSS O3N2 sample. $[\text{Fe}/\text{H}]$ is defined as $[\text{O}/\text{H}] - 0.35$ dex, where $[\text{O}/\text{H}]$ is estimated using the PP04 O3N2 calibration. For all KBSS galaxies, $\text{SFR}_{\text{KE12}} > \text{SFR}(Z)$, with the discrepancy being larger for more metal-poor galaxies.

the effect is significantly smaller than the overall shift towards lower SFR, but is nonetheless significant and can only be accounted for using a metallicity-dependent conversion factor. Since stellar metallicity is being inferred from gas-phase oxygen abundance, the magnitude of the effect is dependent on the calibration used to estimate oxygen abundance. Testing different strong line ratios and calibrations allows us to quantify how this inter-calibration variation can affect the characterization of a M_* - Z_g -SFR correlation.

Given the crucial role of SFR in the formulation of the FMR, one of the principal aims of this paper is to investigate how a Z_* -dependent SFR may impact the detection of the FMR. Throughout the paper, we conduct all of the analysis using both SFR estimates to allow for direct study of the effect of adopting a metallicity-dependent SFR conversion factor as well as comparison with earlier work.

3. THE RELATIONSHIP BETWEEN M_* , METALLICITY, AND SFR

The combination of SFMS and MZR sets the relationship between M_* , Z_g , and SFR. The FMR suggests that the redshift evolution of the SFMS and MZR towards higher SFR and lower Z_g at fixed M_* respectively, can

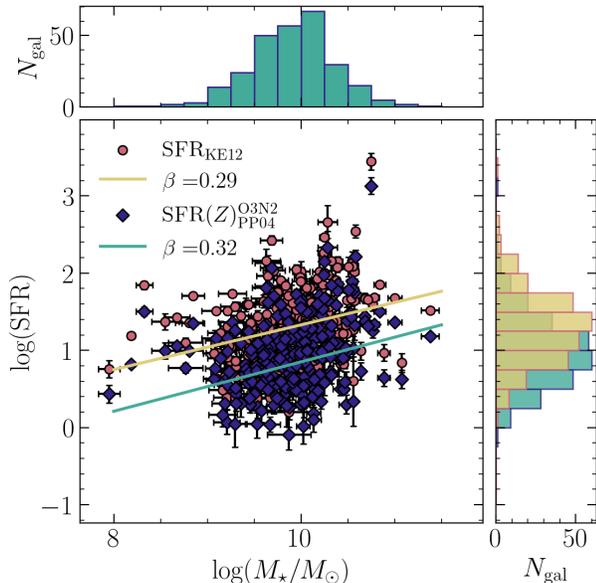


Figure 4. SFR vs. stellar mass for the KBSS O3N2 sample. $\text{SFR}(Z)$ is shown by purple diamonds, with the regression line in teal and SFR_{KE12} is shown by pink circles, with the regression line in yellow. Histograms show the distributions of $\log(M_*)$, $\log(\text{SFR}_{\text{KE12}})$ (yellow), and $\log(\text{SFR}(Z))_{\text{PP04}}^{\text{O3N2}}$ (teal). Adopting $\text{SFR}(Z)$ results in a SFMS with a lower normalization (SFR_{10}) and a slightly steeper slope (β).

be captured by a three-dimensional, redshift-invariant surface in M_* - Z_g -SFR space. The surface is expected to be roughly planar (Mannucci et al. 2010) in the stellar mass and SFR regime probed by KBSS. In the following sections we present two limiting projections of M_* - Z_g -SFR space: the SFMS and MZR. We also search for the projection of least scatter, compare KBSS galaxies to local galaxies, and quantify the anticorrelation between residual metallicity and SFR. Together, these tests comprehensively describe the M_* - Z_g -SFR relationship in KBSS galaxies at $z \sim 2.3$ in relation to the locally defined FMR.

3.1. The Star-Forming Main Sequence

A consequence of adopting a metallicity-dependent SFR conversion factor is a change in the star forming main sequence (SFMS). For each SFR method, we fit a power law to the data with the form

$$\log(\text{SFR}) = \beta \times (\log(M_*) - 10) + \log(\text{SFR}_{10}) \quad (8)$$

where β is the slope of the SFMS and SFR_{10} is the median SFR for a galaxy with a stellar mass of $10^{10} M_\odot$. Here and throughout the paper, we use the PYTHON package LINMIX to simultaneously estimate intrinsic scatter and fit a regression line. This package is adapted from the IDL routine described in Kelly (2007) and employs a Bayesian method designed to handle data with

uncertainties in both the dependent and independent variables and an intrinsic level of scatter.

As can be seen in Figure 4, adopting $\text{SFR}(Z)$ results in a SFMS that is offset towards lower SFR at fixed M_* and has a slightly steeper slope. The scale of the change is dependent on the strong-line calibration being used to derive oxygen abundance, and therefore, the iron abundance. Calibrations that result in the steepest MZR slopes (such as B18) are associated with a marginally steeper SFMS with a lower normalization.

As is the case for all emission-line galaxy surveys, KBSS preferentially observes highly star-forming galaxies. Additionally, we impose SNR limits on the detection of $\text{H}\alpha$, therefore, the slope differs from the shapes reported in the literature using “mass-selected” samples (e.g., Whitaker et al. 2014; Leja et al. 2022). Depending on the choice of strong-line calibration, we recover $0.29 \leq \beta \leq 0.34$, while samples at similar redshifts have been found to have SFMS slopes of 0.91 ($\log(M_*) < 10.2$) and 0.67 ($\log(M_*) > 10.2$) (Whitaker et al. 2014). The slopes we recover for KBSS galaxies are robust to outlier detection methods: when we use both random sample consensus (RANSAC) and jack-knifing, the slope remains statistically similar. When adopting SFR_{KE12} , the normalization of our SFMS ($\log(\text{SFR}_{10}) = 1.33$) is comparable to the SFR at $\log(M_*) = 10$ predicted by Whitaker et al. (2014, $\log(\text{SFR}_{10}) = 1.44$). However, adopting $\text{SFR}(Z)$ leads to a significantly lower normalization ($\log(\text{SFR}_{10}) \sim 0.85$). The $\text{SFR}(Z)$ SFMS is well-aligned with the SFMS predicted at $z \sim 2$ by hydrodynamical simulations (Torrey et al. 2014; Donnari et al. 2019), which tend to be offset towards a slightly lower SFR at fixed stellar mass when compared to the observed SFMS. Considering a metallicity dependence may therefore result in significantly lower normalizations of the SFMS in mass-selected samples.

3.2. The Mass-Metallicity Relation

The eight different strong-line calibrations produce significantly different MZR slopes, scatters, and normalizations (see Figure 5). For each calibration, we fit a power-law in the form

$$12 + \log(\text{O}/\text{H}) = \gamma \times (\log(M_*) - 10) + Z_{10} + \mathcal{N}(0, \sigma_{\text{int}}) \quad (9)$$

In the case of O3N2-based oxygen abundance, the slope can be as high as $\gamma = 0.21 \pm 0.02$ when using the B18 calibration or as low as $\gamma = 0.11 \pm 0.01$ when using either the M13 or S18 calibration. The normalization varies by 0.224 dex between different calibrations, where the photoionization model-based B18 calibration produces the highest normalization ($Z_{10} = 8.499 \pm 0.009$) and the M13 calibration produces the lowest normal-

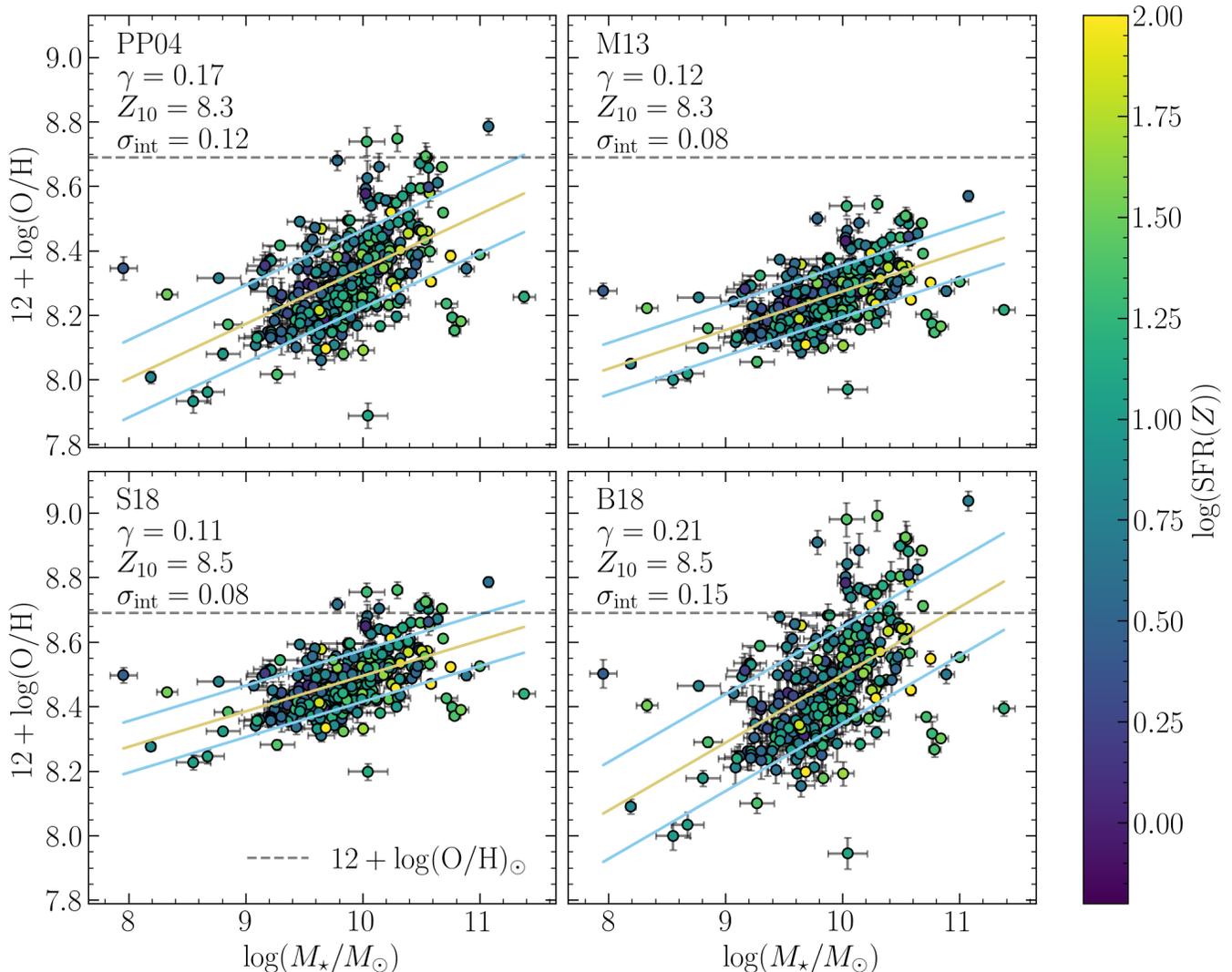


Figure 5. Gas-phase oxygen abundance vs. stellar mass for the KBSS O3N2 sample. The regression line is shown in yellow, intrinsic scatter is shown in light blue, individual galaxies are color-coded by $\log(\text{SFR}(Z))$, and $12 + \log(\text{O}/\text{H})_\odot = 8.69$ is shown by a gray dashed line. Each panel uses a different O3N2 calibration. Clockwise from top left: PP04, M13, B18, and S18. The slope (γ), normalization (Z_{10}), and scatter (σ_{int}) of the MZR differ significantly depending on the chosen strong-line calibration.

ization ($Z_{10} = 8.275 \pm 0.005$). N2-based MZR tend to have slightly shallower slopes and less scatter than O3N2-based MZR. Across both strong-line ratios, calibrations with a larger $|B|$ value (see Table 1) result in steeper MZR, with more scatter. For a summary of our MZR results, see Table 3 and Figure 5.

Testing calibrations that result in different underlying MZR shapes allows us to determine whether the detection of the FMR is sensitive to the MZR slope and scatter, as well as the choice of line ratio. Other studies have chosen to look for the FMR in line ratio space (e.g., Sanders et al. 2018), which has a similar effect of ensuring the detection of the FMR is not reliant on the MZR shape.

3.3. Parametric Method

Mannucci et al. (2010) originally described the FMR as a three-dimensional curved surface in gas phase oxygen abundance, stellar mass, SFR space. Different two-dimensional projections of this surface can be represented by the parameter $\mu_\alpha \equiv \log(M_\star) - \alpha \log(\text{SFR})$ where α has a value between -1 and 1 , with $\alpha = 0$ corresponding to the MZR, $\alpha = 1$ corresponding to a direct relationship between metallicity and sSFR, and intermediate values corresponding to intermediate projections. Mannucci et al. (2010) found the two-dimensional projection of the three-dimensional FMR that minimizes scatter at $\alpha_{\text{min}} = 0.32$. This parametric approach has been applied with varying results at a range of redshifts

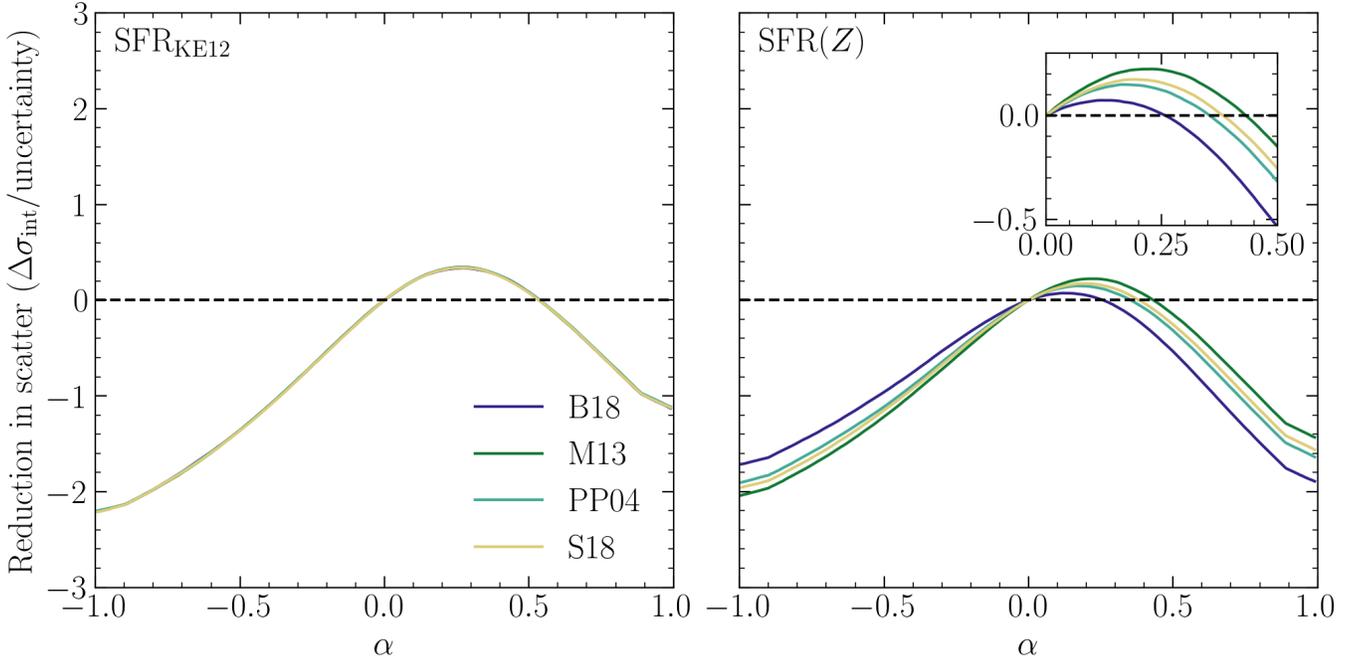


Figure 6. Reduction in intrinsic scatter vs. α for the four O3N2 strong-line calibrations and using SFR_{KE12} (left panel) and $\text{SFR}(Z)$ (right panel). The ordinate is specifically defined as the reduction in intrinsic scatter ($\Delta\sigma_{\text{int}}$), relative to the MZR scatter, divided by the uncertainty on the intrinsic scatter. The inset panel zooms in to $0 \leq \alpha \leq 0.5$ to show the effect of adopting $\text{SFR}(Z)$. Scatter is not significantly reduced at any value of α . See Appendix A for results using N2 calibrations.

Table 3. Summary of MZR properties for different strong-line calibrations. We report the slope (γ), normalization (Z_{10}), intrinsic scatter (σ_{int}), and the associated uncertainties.

Calibration	γ	Z_{10}	σ_{int}
PP04, O3N2	0.17 ± 0.02	8.344 ± 0.008	0.12 ± 0.04
M13, O3N2	0.12 ± 0.01	8.275 ± 0.005	0.08 ± 0.03
B18, O3N2	0.21 ± 0.02	8.499 ± 0.009	0.15 ± 0.05
S18, O3N2	0.11 ± 0.01	8.496 ± 0.005	0.08 ± 0.02
M13, N2	0.14 ± 0.01	8.378 ± 0.006	0.10 ± 0.03
S14, N2	0.11 ± 0.01	8.338 ± 0.005	0.08 ± 0.02
B18, N2	0.14 ± 0.02	8.436 ± 0.007	0.11 ± 0.03
S18, N2	0.10 ± 0.01	8.504 ± 0.005	0.07 ± 0.02

(Yates et al. 2012; Andrews & Martini 2013; Curti et al. 2020; Sanders et al. 2021) and it remains an open question whether the projection of least scatter is redshift-invariant (Garcia et al. 2024a).

We follow a similar method to Mannucci et al. (2010) and define the abscissa by the variable $\mu_\alpha \equiv \log(M_\star) - \alpha \log(\text{SFR})$. We sample values of α between -1 and 1 in steps of 0.01 . At each step, we fit a regression line to the data in the form

$$12 + \log(\text{O}/\text{H}) = \gamma \times \mu_\alpha + Z_0 + \mathcal{N}(0, \sigma_{\text{int}}) \quad (10)$$

and estimate the intrinsic scatter using LINMIX. Since LINMIX results have some stochasticity, we apply a box-car smoothing function to the intrinsic scatter values, smoothing over a window of ± 0.1 in α .

Across all strong-line calibrations, SFR calculation methods, and means of estimating intrinsic scatter, we find no statistically significant reduction in scatter at $\alpha \neq 0$. Figure 6 shows the results of the parametric analysis using the O3N2 sample and either SFR_{KE12} (left panel) or $\text{SFR}(Z)$ (right panel). The ordinate is defined as the reduction in scatter, measured relative to the scatter of the MZR ($\Delta\sigma_{\text{int}}$) and divided by the uncertainty on intrinsic scatter. In the left panel of Figure 6, the solid curves (where each color represents a different strong-line calibration) peak around $\alpha \sim 0.3$ and in the right panel, the curves peak between $0.1 \lesssim \alpha \lesssim 0.2$, showing that scatter is ostensibly minimised at $\alpha \neq 0$. However, the uncertainty on the intrinsic scatter is such that any reduction in scatter is not statistically significant. It is worth noting that while all of the curves in the left panel of Figure 6 overlap, the absolute reduction in scatter does differ by calibration. Calibrations that more heavily weight the line ratio (larger B in Table 1) show a larger reduction in scatter, albeit with a larger uncertainty on the scatter. Hence, when we normalise the reduction in scatter by the uncertainty, all of the curves collapse onto one another.

We find a similar result using N2-based calibrations, although the relative reduction in scatter is smaller and peaks at a lower value of α . Given that O3N2 has been shown to produce oxygen abundances in better agreement with direct T_e abundances in KBSS (Steidel et al. 2014) and the consistency between our O3N2- and N2-based results, we do not include further results using the N2 calibrations in the main body of the paper. For further detail regarding the N2 calibration results, we refer the reader to Appendix A.

As a point of comparison, we also employ the same method used in the original Mannucci et al. (2010) paper, where we consider the dispersion in $\log(\text{O}/\text{H})$ about the best-fit MZR. To estimate the uncertainty in the dispersion, we perturb each point in both $12 + \log(\text{O}/\text{H})$ and $\mu_{0.32}$ (the projection at which dispersion is minimized) 100 different times, drawing the perturbation from a normal distribution with a standard deviation equal to the measurement uncertainty. Then, we take the standard deviation of the simulated dispersion measurements as the uncertainty on the dispersion. Our results are unchanged when we measure total dispersion (uncorrected for observational uncertainty), as in Mannucci et al. (2010), as opposed to intrinsic scatter. Therefore, we conclude that the discrepancy between our result and the Mannucci et al. (2010) result is not due to choice of method, but reflects intrinsic differences between local galaxy samples and KBSS galaxies.

3.4. Comparison to the Local FMR

It is possible that KBSS galaxies lie on the FMR but in an area of M_\star - Z_g -SFR space where the dependence on SFR is weak and a significant reduction in scatter is too subtle to be measured. To determine if this is the case, we compare KBSS galaxies to $z \sim 0$ galaxies that have been used to define the local FMR. Specifically, we use the stacked SDSS spectra from Andrews & Martini (2013), with M_\star and SFR rescaled to a Chabrier (2003) IMF. To allow for the most direct comparison, we consider $12 + \log(\text{O}/\text{H})$ calculated from O3N2 PP04 for both KBSS and SDSS galaxies. For this calibration, Andrews & Martini (2013) report that scatter is minimized at $\alpha_{\min} = 0.32$, and we show this projection in the left panel of Figure 7. However, there is still a noticeable SFR gradient in the Andrews & Martini (2013) stacks at this projection, suggesting that it is perhaps not the optimal projection. In the right panel of Figure 7, we use $\mu_{0.66} = \log(M_\star) - 0.66 \times \log(\text{SFR})$ as the abscissa instead. Andrews & Martini (2013) report that scatter is minimized at $\alpha_{\min} = 0.66$ when using direct method T_e abundances. As can be seen in Figure 7, the trend in SFR is reduced at this projection. However,

stacks with high SFR are pushed to low $\mu_{0.66}$ and have very large scatter from the otherwise tight series in oxygen abundance and $\mu_{0.66}$. These highly scattered points may explain why scatter is technically minimized at a lower value of α , despite there still being a visible trend in SFR.

In the left panel of Figure 7, KBSS galaxies are offset towards lower $12 + \log(\text{O}/\text{H})$ at fixed $\mu_{0.32}$ compared to the $z \sim 0$ SDSS galaxies. The offset is slightly larger when using $\text{SFR}(Z)$ due to the bulk offset between SFR_{KE12} and $\text{SFR}(Z)$. In the right panel of Figure 7, KBSS and SDSS appear to overlap.

However, we caution that an overlap in $\log(\text{O}/\text{H})$ - $\mu_{0.66}$ space does not necessarily imply that KBSS and SDSS fall on a shared fundamental plane in M_\star - Z_g -SFR space. In Section 4.2, we further discuss how our results differ from predictions associated with a redshift-invariant FMR plane, demonstrating that the overlap between KBSS and SDSS is not due to a shared plane.

3.5. Non-Parametric Method

A complementary, non-parametric approach was proposed by Salim et al. (2014), who did not adopt the Mannucci et al. (2010) parametrization of the FMR. Instead, Salim et al. (2014) quantified the anticorrelation between oxygen abundance and the offset of a galaxy from the star forming main sequence. Salim et al. (2014) argued that this method is more physically motivated, as it considers the relationship between Z_g and the galaxy's residual specific star formation rate (sSFR), relative to the typical sSFR for a galaxy of the same mass, rather than absolute SFR, and does not require the surface in M_\star - Z_g -SFR to be a plane. Various non-parametric approaches have been employed to investigate the M_\star - Z_g -SFR relation, generally comparing residual oxygen abundance ($\Delta \log(\text{O}/\text{H})$), defined as the difference between a galaxy's oxygen abundance and the expected oxygen abundance for a galaxy of the same stellar mass, with a third, SFR-based parameter (e.g., Sanders et al. 2021; Topping et al. 2021). The FMR does predict that $\Delta \log(\text{O}/\text{H})$ will be anticorrelated with SFR, although it should be noted that an anticorrelation between $\Delta \log(\text{O}/\text{H})$ and SFR is not necessarily consistent with the FMR plane defined by Mannucci et al. (2010), an issue we discuss further in Section 4.1.

Here we consider two versions of the non-parametric approach: first, we quantify the correlation between residual oxygen abundance and absolute SFR. Residual oxygen abundance is calculated relative to the power law (Equation 9) parametrization of the MZR for each calibration (summarized in Table 3) such that $\Delta \text{MZR} \equiv (12 + \log(\text{O}/\text{H})) - (\gamma \times (\log(M_\star) - 10) + Z_{10})$. We then

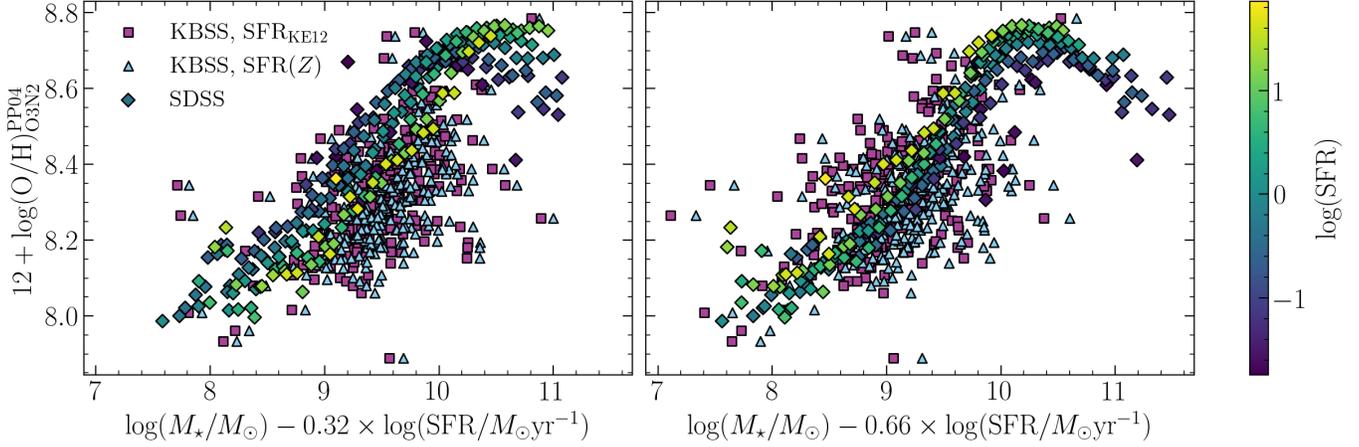


Figure 7. Oxygen abundance vs. μ_α for SDSS galaxies (diamonds, color-coded by SFR, from Andrews & Martini 2013) and KBSS galaxies (purple squares for SFR_{KE12} and light blue triangles for $\text{SFR}(Z)$). The left panel plots $\mu_{0.32}$ and the right panel plots $\mu_{0.66}$. On the left, KBSS galaxies are offset towards lower oxygen abundances at fixed $\mu_{0.32}$. On the right, KBSS galaxies and SDSS galaxies overlap, although scatter is not reduced for KBSS galaxies at this projection.

use LINMIX to perform a linear regression on the residual oxygen abundance and SFR and report the Spearman’s rank correlation coefficient, ρ , and p -value.

Secondly we quantify the correlation between $\Delta \log(\text{O}/\text{H})$ and the relative sSFR, following the method outlined by Salim et al. (2014). First, we characterise the mass-sSFR relationship for KBSS galaxies, and use the regression line to calculate the residual sSFR for each galaxy ($\Delta \text{sSFR} \equiv \text{sSFR} - \langle \text{sSFR}(M_*) \rangle$). Similarly, we use LINMIX to perform a linear regression and report ρ and p . The resulting $\Delta \log(\text{O}/\text{H})$ -SFR and $\Delta \log(\text{O}/\text{H})$ - ΔsSFR correlations can be seen in Figures 8 and 9 respectively.

Across calibrations, we find a weak but significant ($p < 0.02$) anticorrelation between residual oxygen abundance ($\Delta \log(\text{O}/\text{H})$) and SFR_{KE12} . We also observe a weak but significant ($p < 0.009$) anticorrelation between $\Delta \log(\text{O}/\text{H})$ and $\Delta \text{sSFR}_{\text{KE12}}$. See Table 4 for a full list p -values and Spearman ρ coefficients by calibration and SFR calculation. While the $\Delta \log(\text{O}/\text{H})$ - ΔsSFR slopes recovered for KBSS (yellow and purple lines in Figure 9) are significantly shallower than what has been found at $z \sim 2.3$ by Sanders et al. (2018, $\psi_2 = -0.14$, see also Appendix B), the scatter in KBSS galaxies is large enough that Sanders et al. (2018) slope could be consistent with KBSS.

However, when adopting $\text{SFR}(Z)$, the correlation is weaker and only marginally significant or consistent with a null result. The difference between the the results for the two SFR methods is easily understood. While the principal effect of adopting $\text{SFR}(Z)$ is a systematic shift towards lower SFR for all galaxies, the effect is larger for more metal-poor galaxies and smaller for more metal-rich galaxies (see Figure 3). Therefore, a set of galaxies

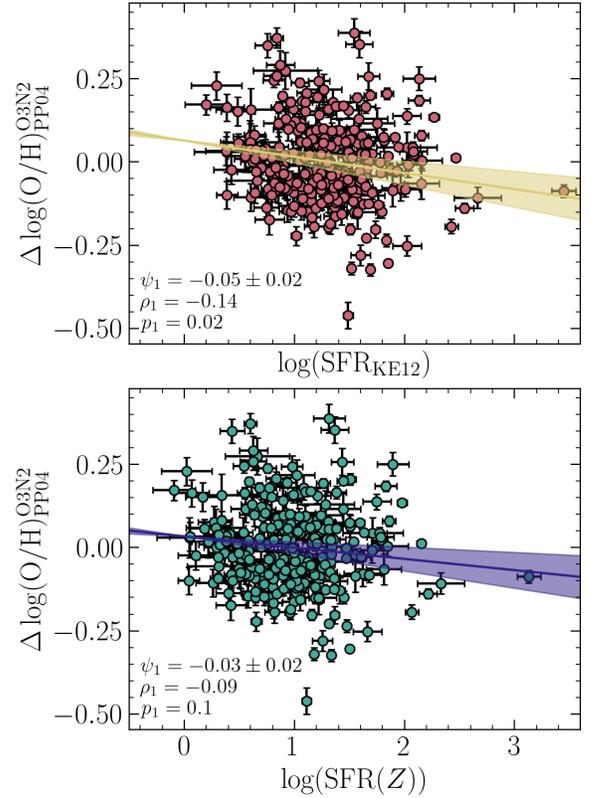


Figure 8. *Top:* $\Delta \log(\text{O}/\text{H})$ vs. $\log(\text{SFR}_{\text{KE12}})$ for the KBSS O3N2 sample. *Bottom:* as above, but using $\log(\text{SFR}(Z))$. There is a weak and marginally significant anticorrelation between $\Delta \log(\text{O}/\text{H})$ and SFR in the top panel, and no significant correlation in the bottom panel. The trend is seen across calibrations, here we show the results for the PP04 calibration.

Table 4. The slope (ψ_1 , ψ_2), Spearman’s rank correlation coefficient (ρ_1 , ρ_2), p -value (p_1 , p_2) for the $\Delta\text{MZR}_{\text{O3N2}}$ -SFR and $\Delta\text{MZR}_{\text{O3N2}}$ - ΔsSFR anticorrelations respectively.

Calibration	SFR	$\Delta\log(\text{O}/\text{H})$ -SFR			$\Delta\log(\text{O}/\text{H})$ - ΔsSFR		
		ψ_1	ρ_1	p_1	ψ_2	ρ_2	p_2
PP04	KE12	-0.05 ± 0.02	-0.14	0.02	-0.05 ± 0.02	-0.16	0.009
PP04	Z	-0.03 ± 0.02	-0.09	0.1	-0.03 ± 0.02	-0.11	0.08
M13	KE12	-0.04 ± 0.01	-0.15	0.01	-0.04 ± 0.01	-0.16	0.009
M13	Z	-0.03 ± 0.01	-0.12	0.05	-0.03 ± 0.01	-0.13	0.03
B18	KE12	-0.06 ± 0.02	-0.14	0.02	-0.06 ± 0.02	-0.16	0.009
B18	Z	-0.03 ± 0.02	-0.06	0.32	-0.03 ± 0.02	-0.08	0.2
S18	KE12	-0.03 ± 0.01	-0.14	0.02	-0.03 ± 0.01	-0.16	0.009
S18	Z	-0.02 ± 0.01	-0.09	0.12	-0.02 ± 0.01	-0.11	0.07

which show an anticorrelation between residual oxygen abundance and SFR_{KE12} will have this correlation weakened by the adoption of $\text{SFR}(Z)$. Conversely, a more metal-poor galaxy will produce more $\mathcal{L}_{\text{H}\alpha}$ than a more metal-rich galaxy with the same SFR and stellar mass. Assuming a constant conversion factor would, however, suggest that the more metal-poor galaxy is more highly star-forming, introducing an artificial anticorrelation between oxygen abundance and SFR. By the same logic, we can understand why the calibration with the steepest MZR slope, B18, results in the largest suppression of the anticorrelation when switching from SFR_{KE12} to $\text{SFR}(Z)$.

The p -values for both the $\Delta\log(\text{O}/\text{H})$ - $\text{SFR}(Z)$ and $\Delta\log(\text{O}/\text{H})$ - $\Delta\text{sSFR}(Z)$ anticorrelations are such that we cannot rule out a M_\star - Z_g - $\text{SFR}(Z)$ relation. Moreover, the strength of the correlation is clearly dependent on the MZR slope, the “true” value of which remains poorly constrained. Thus, it remains uncertain whether a M_\star - Z_g - $\text{SFR}(Z)$ relation exists in KBSS galaxies, but it is evident that a constant SFR conversion factor (such as the KE12 conversion, although this trend will be seen for any constant conversion factors) can result in an overestimate of the correlation strength.

N2-based calibrations yield similar results: $\Delta\log(\text{O}/\text{H})$ is marginally and weakly anticorrelated with both SFR and ΔsSFR . Further detail and figures illustrating this can be found in Appendix A. For both SFR_{KE12} and $\text{SFR}(Z)$, the anticorrelation with $\Delta\log(\text{O}/\text{H})_{\text{N2}}$ is weaker than the anticorrelation with $\Delta\log(\text{O}/\text{H})_{\text{O3N2}}$ (cf. Tables 4 and 5). The discrepancy highlights that strong-line calibrations are not self-consistent and are sensitive to metallicity in different ways. At fixed stellar mass, N2 is less strongly correlated with SFR than O3N2. Any correlation between a strong line ratio and SFR may be indicative of a correlation between metallicity and SFR, or an independent correlation between the line ratio and SFR. Our analysis

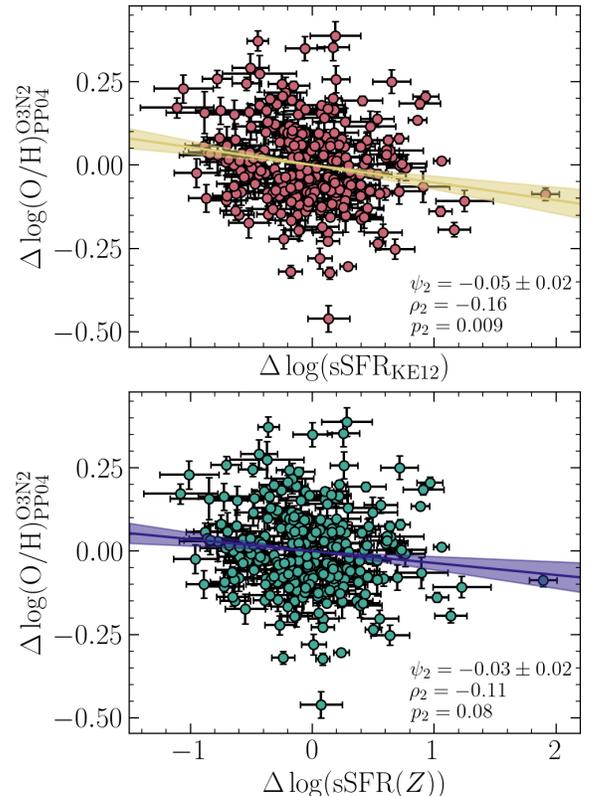


Figure 9. *Top:* $\Delta\log(\text{O}/\text{H})$ vs. $\Delta\text{sSFR}_{\text{KE12}}$ for the KBSS O3N2 sample. *Bottom:* as above, but using $\Delta\text{sSFR}(Z)$. A weak and marginally significant $\Delta\log(\text{O}/\text{H})$ - ΔsSFR anticorrelation is observed only when using SFR_{KE12} . As in Figure 8, we use the PP04 calibration, but this result is observed across calibrations.

cannot differentiate between these two situations, only show that the strength of the correlation varies between line ratios.

4. DISCUSSION

4.1. Reconciling Results From Parametric and Non-Parametric Methods

At face value, it would seem contradictory to observe a M_\star - Z_g -SFR relation without a corresponding projection of least scatter. Given that the presence of the FMR is sometimes reported based on $\Delta \log(\text{O}/\text{H})$ -SFR or ΔMZR - ΔsSFR correlations (e.g., Topping et al. 2021), it's important to understand how a M_\star - Z_g -SFR relation may or may not imply a reduction in intrinsic scatter.

To explore the relationship between the parametric and non-parametric methods, we use an injection-recovery test, where we input simulated data based on an artificial M_\star - Z_g -SFR relationship into the parametric analysis method. For each realization of the data, we measure the reduction in scatter for $0 \leq \alpha \leq 1$.

The injected data has the same mass and SFR distribution as the KBSS O3N2 sample, using SFR_{KE12} . Each data point is assigned a residual metallicity based on a constructed $\Delta \log(\text{O}/\text{H})$ -SFR relationship, which takes the form of

$$\Delta \log(\text{O}/\text{H}) = \psi_1 \times \log(\text{SFR}) + \mathcal{N}(0, \sigma_{\text{int}}) + \mathcal{N}(0, \sigma_{\text{meas}}) \quad (11)$$

where ψ_1 is the slope, σ_{int} is intrinsic scatter in the $\Delta \log(\text{O}/\text{H})$ -SFR relationship, and σ_{meas} is the measurement uncertainty. We assume a constant value of $\sigma_{\text{meas}} = 0.03$, equal to the median measurement uncertainty on $\Delta \log(\text{O}/\text{H})$ in the O3N2 sample using the PP04 calibration. Without loss of generality, we define $\Delta \log(\text{O}/\text{H}) = 0$ at $\log(\text{SFR}) = 0$. The value of $\Delta \log(\text{O}/\text{H})$ is then added to the value of $\log(\text{O}/\text{H})$ predicted by the power law form of the MZR (Equation 9), given the associated stellar mass. ψ_1 and σ_{int} are both varied to produce the simulated data sets. For each realization of the data, we then use the same parametric method described in Section 3.3 to find the value of α that minimizes scatter and measure the reduction in scatter, relative to the MZR ($\alpha = 0$).

Figure 10 shows the results of our injection-recovery test. Each pixel represents a simulated dataset which was constructed according to Equation 11 with a different value of ψ_1 and σ_{int} . The color of each pixel shows the reduction in intrinsic scatter, relative to the MZR scatter, divided by the uncertainty. A significant reduction ($> 3\sigma$) in scatter can only be observed alongside a significantly steeper $\Delta \log(\text{O}/\text{H})$ -SFR relation, regardless of the intrinsic scatter in the relationship. In fact, ψ_1 must be at least 2.4 times steeper than ψ_{KBSS} before a significant reduction in scatter is measured. Hence, an anticorrelation between residual metallicity and SFR is only associated with a significant reduction in scatter if the anticorrelation is much stronger than what we measure in KBSS. Indeed, the MOSDEF sample shows a stronger $\Delta \log(\text{O}/\text{H})$ -SFR anticorrelation (see Figure 18

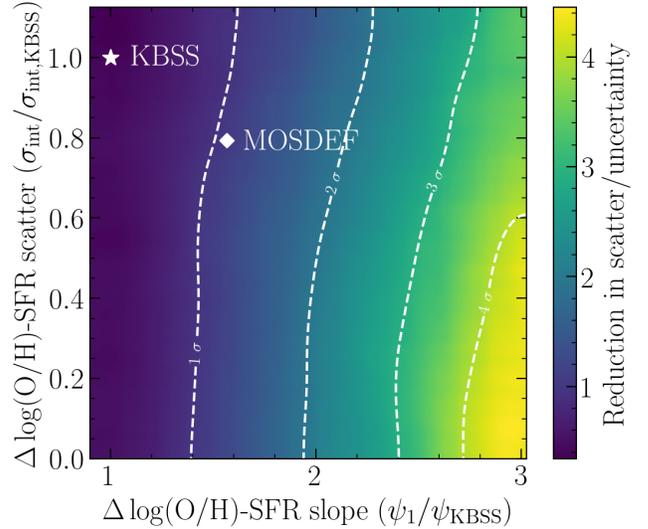


Figure 10. $\Delta \log(\text{O}/\text{H})$ -SFR scatter vs. $\Delta \log(\text{O}/\text{H})$ -SFR slope of the simulated datasets, color-coded by reduction in scatter at α_{min} . Slope and scatter have been normalized by $\psi_{\text{KBSS}} = -0.05$ and $\sigma_{\text{int,KBSS}} = 0.13$ respectively (shown by the white star), and reduction in FMR scatter is normalized by the uncertainty (σ) on the FMR scatter. The MOSDEF slope and scatter are shown by white diamond. A significant reduction in scatter is only reliably measured at steeper ψ_1 , showing that conclusions drawn from parametric and non-parametric methods are not necessarily consistent.

and Appendix B) with less scatter. Values of ψ_1 and σ_{int} for MOSDEF are marked on Figure 10 by a white diamond. At these values, our injection recovery tests predict a marginal, $\sim 1.2\sigma$ reduction in scatter. Applying our parametric analysis method to MOSDEF (see Figure 16) yields a $\sim 1.5\sigma$ reduction in scatter at α_{min} . Similarly, the SDSS stacks from Andrews & Martini (2013) show a significant reduction in scatter at α_{min} and have much steeper $\Delta \log(\text{O}/\text{H})$ -SFR slope ($\psi_1 = -0.22 \pm 0.02$, over four times steeper than KBSS).

The same conclusion can be reached analytically. Assuming there is a significant $\Delta \log(\text{O}/\text{H})$ -SFR anticorrelation, total MZR scatter (σ_{tot}) can be decomposed into three components:

$$\sigma_{\text{tot}}^2 = (\psi_1 \sigma_{\text{SFR}})^2 + \sigma_{\text{int}}^2 + \sigma_{\text{meas}}^2 \quad (12)$$

where σ_{meas} is scatter due to measurement error in $\log(\text{O}/\text{H})$, σ_{int} is the intrinsic scatter in the $\Delta \log(\text{O}/\text{H})$ -SFR correlation (ordinate of Figure 10), ψ_1 is the slope of the $\Delta \log(\text{O}/\text{H})$ -SFR correlation (abscissa of Figure 10), and σ_{SFR} is the standard deviation of $\log(\text{SFR})$. When we estimate the total intrinsic scatter using LINMIX, we are estimating the combination of $\psi_1 \sigma_{\text{SFR}}$ and σ_{int} . In the case of very shallow $\Delta \log(\text{O}/\text{H})$ -SFR anticorrelations, as is seen in KBSS, the total intrinsic scatter is dominated by the scatter in $\Delta \log(\text{O}/\text{H})$ -SFR. The

parametric approach solves for the value of α which minimizes the contribution of $\psi_1\sigma_{\text{SFR}}$ to the total intrinsic scatter (i.e., when $\alpha_{\text{min}} = \psi_1/\gamma$). However, in KBSS, $\psi_1\sigma_{\text{SFR}}$ is very small to begin with, resulting in no significant reduction in scatter. Indeed in Figure 10, we only begin to see a significant reduction in scatter when ψ_1 is much steeper than ψ_{KBSS} .

4.2. Comparison to Other Samples

Figure 7 shows that depending on the choice of μ_α , KBSS may or may not appear to overlap with local galaxies. If we choose $\mu_{0.32}$, which Andrews & Martini (2013) states reduces scatter when using the PP04 calibration, KBSS galaxies are offset from the locally-defined FMR towards lower oxygen abundances at fixed $\mu_{0.32}$. But, if we choose $\mu_{0.66}$, which reduces scatter of $z \sim 0$ galaxies when using direct-method T_e abundances (Andrews & Martini 2013), KBSS galaxies appear to fully overlap with SDSS stacks.

Although KBSS and SDSS do overlap in the right panel of Figure 7, this does not necessarily mean that they occupy the same plane in M_\star - Z_g -SFR space. Indeed, we can see from Figure 6 that scatter is nominally increased for KBSS galaxies at $\alpha = 0.66$. $\mu_{0.66}$ may not be the projection of least scatter for KBSS galaxies, just a projection at which KBSS and SDSS galaxies overlap. If KBSS and SDSS were on a fundamental, redshift-invariant plane in M_\star - Z_g -SFR space, then we would expect scatter to be minimized at the same value of α at all redshifts.

However, as has been noted in Sections 3.3 and 4.1, the uncertainty on scatter is such that we don't see a significant reduction in scatter at *any* value of α . Therefore, it's difficult to argue that we have found a different value of α_{min} for KBSS galaxies compared to $\alpha = 0.66$. Additionally, the increase in KBSS galaxy scatter at $\alpha = 0.66$ is also not statistically significant. We can attempt to analytically determine α_{min} : as was noted in Section 4.1, α_{min} minimizes the contribution of SFR to the total scatter in $\log(\text{O}/\text{H})$. Assuming that α_{min} completely cancels out the dependence in $\Delta \log(\text{O}/\text{H})$ on SFR, $\alpha_{\text{min}} = -\psi_1/\gamma$, where ψ_1 is the slope of the $\Delta \log(\text{O}/\text{H})$ -SFR correlation and γ is the MZR slope. Using γ and ψ_1 values found using the O3N2 PP04 calibration and SFR_{KE12} yields $\alpha_{\text{min}} = 0.3 \pm 0.1$, suggesting that $\alpha = 0.66$ is not the optimal projection for KBSS. Neither value of α that can simultaneously reduce scatter in both SDSS and KBSS, suggesting that they do not occupy a common plane.

Indeed, Garcia et al. (2024a) finds that three different hydrodynamical simulations: Illustris (Torrey et al. 2014), IllustrisTNG (Nelson et al. 2019), and

EAGLE (McAlpine et al. 2016) all show evidence for a redshift-evolving value of α_{min} . Within our framework, this observation is consistent with a significant but redshift-dependent M_\star - Z_g -SFR relation (which Garcia et al. 2024a, refers to as a ‘‘weak’’ FMR) rather than a redshift-invariant FMR. Our finding that scatter in KBSS galaxies is not reduced at the same projection as SDSS galaxies ($\alpha = 0.66$) suggests that an FMR does not exist, irrespective of whether the galaxies overlap in the right panel of Figure 7.

The analysis in Section 4.1 and the discussion in Garcia et al. (2024a) both highlight the connection between parametric and non-parametric methods. An FMR should produce redshift-invariant values of α_{min} and ψ_1 (the slope of the $\Delta \log(\text{O}/\text{H})$ -SFR correlation Garcia et al. 2024a). Measuring $\Delta \log(\text{O}/\text{H})$ from the non-linear fit to the MZR reported in Andrews & Martini (2013), we find $\psi_1 = -0.22 \pm 0.02$ for SDSS stacks. This slope is over four times steeper than the steepest slope found for KBSS galaxies (using PP04 and SFR_{KE12} , see Table 4). The redshift evolution of ψ_1 is highly significant and shows that the strength with which SFR determines MZR scatter (see Equation 11) varies with redshift.

Comparing KBSS to SDSS therefore demonstrates that although $z \sim 0$ and $z \sim 2.3$ galaxies may overlap in certain projections of M_\star - Z_g -SFR space, they are not on the same three-dimensional plane. The results of Section 3.3 show tenuous evidence for the redshift evolution of α_{min} , and the results of Section 3.5 show strong evidence that ψ_1 is not redshift invariant. A redshift-invariant FMR cannot account for such evolution in ψ_1 implying that the M_\star - Z_g -SFR relation must evolve with redshift.

In Figure 11, we plot the mean offset between different galaxy samples and the locally defined FMR. In the left-hand panel, we define the FMR by a linear fit to SDSS galaxies in the $\mu_{0.32}$ - $12 + \log(\text{O}/\text{H})$ plane (left panel of Figure 7). We restrict the fit to galaxies with $\mu_{0.32} < 10.4$ as the trend becomes non-linear at higher $\mu_{0.32}$. In the right-hand panel, we define the FMR using $\mu_{0.66}$ (right panel of Figure 7) instead and restrict the linear fit to galaxies with $\mu_{0.66} < 10$.

As well as the KBSS galaxies analyzed in this paper, we plot the offsets of zCOSMOS (Cresci et al. 2012), MOSDEF ($z \sim 1.5$, Topping et al. 2021, $z \sim 2.3$ and $z \sim 3.3$, Sanders et al. 2021), Onodera et al. (2016), AMAZE (Troncoso et al. 2014), Nakajima et al. (2023), and Curti et al. (2023). Where possible, we use the median oxygen abundances or offsets reported in the paper, along with their associated uncertainties (Cresci et al. 2012; Troncoso et al. 2014; Nakajima et al. 2023). In the

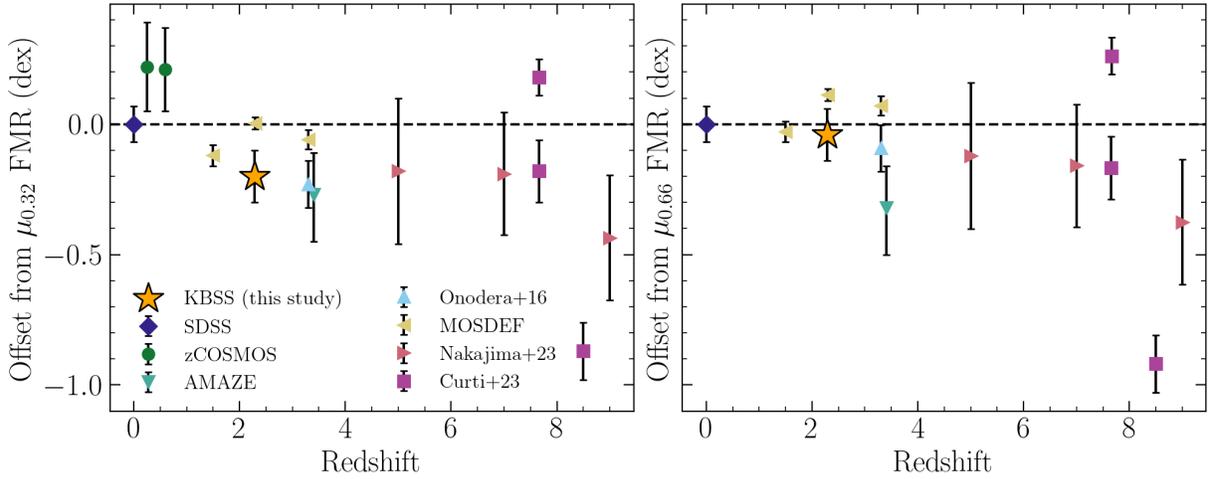


Figure 11. *Left:* Offset from local galaxies at $\mu_{0.32}$ vs. redshift for the KBSS O3N2 sample (orange star), SDSS (purple diamond, Andrews & Martini 2013), zCOSMOS (green circles, Cresci et al. 2012), AMAZE (teal triangle, Troncoso et al. 2014), Onodera et al. (2016, light blue triangle), MOSDEF (yellow triangles, Sanders et al. 2021; Topping et al. 2021), Nakajima et al. (2023, pink triangles), and individual galaxies from Curti et al. (2023, magenta squares). *Right:* As in the left-hand panel, but with offset from local galaxies as $\mu_{0.66}$. While adopting $\mu_{0.66}$ bring KBSS closer to local galaxies, this is not true for all samples. Therefore, there is not a single value of α that minimizes scatter across redshift.

case of Onodera et al. (2016) and MOSDEF, we use the properties reported for composite spectra to estimate the mean offset from the FMR and take the uncertainty as the mean uncertainty on $12 + \log(\text{O}/\text{H})$ from the composite spectra. We plot the offset for the three individual objects with a direct-method oxygen abundance measurement (SMACS0723-ID4590, 6355, and 10612 from Curti et al. 2023).

The galaxy samples shown here use a variety of methods to estimate oxygen abundance: some report direct-method T_e -based abundances (Curti et al. 2023) and many of use strong-line calibrations, other than PP04 (Cresci et al. 2012; Troncoso et al. 2014; Onodera et al. 2016; Sanders et al. 2018; Nakajima et al. 2023). We measure FMR offset from the same sample of local galaxies, but recognize that the exact value of individual FMR offsets depends on how $12 + \log(\text{O}/\text{H})$ and SFR are determined. When adopting $\mu_{0.32}$, KBSS galaxies are offset from the local galaxies (also see the left-hand panel of Figure 7), following a trend that was previously only reported at $z \gtrsim 3.3$ (Troncoso et al. 2014; Onodera et al. 2016). The size of the offset is comparable to the offsets measured at higher redshifts, which show systematically lower $12 + \log(\text{O}/\text{H})$ than predicted by the $z \sim 0$ FMR. When adopting $\mu_{0.66}$, KBSS galaxies are in better agreement with local galaxies. However, this trend is not seen across all samples: for example, MOSDEF at $z \sim 2.3$ and AMAZE are more offset at $\mu_{0.66}$ than at $\mu_{0.32}$. This aligns with our conclusion that although KBSS does overlap with SDSS at $\mu_{0.66}$, this is not because $\alpha_{\min} = 0.66$ effectively decreases scatter at

all redshifts. Indeed, Figure 11 shows that neither value of α_{\min} successfully minimizes scatter and FMR offset across redshift.

Our results appear to be in tension with results from the MOSDEF survey (Kriek et al. 2015), which has been found to be consistent with the FMR at $z \sim 1.5$ (Topping et al. 2021), $z \sim 2.3$, and $z \sim 3.3$ (Sanders et al. 2021). Given the similarity between the two samples, this is initially surprising. One possibility is that the different selection techniques and survey strategies have resulted in the two surveys probing distinct galaxy populations.

KBSS galaxies are selected on the basis of their UV color, targeting Lyman Break analogs (see Adelberger et al. 2004; Steidel et al. 2004, for further detail), and therefore more highly star-forming, and less dust-obscured galaxies are preferentially observed. The inclusion of galaxies selected according to their \mathcal{R} - K color somewhat alleviates this bias (Strom et al. 2018, Strom et al., in prep). In contrast, MOSDEF galaxies are selected based on photo- z estimates which use the Balmer break (Kriek et al. 2015), and therefore the sample may be biased towards more mature galaxies. Additionally, due to the difference in observing strategies, individual KBSS galaxies span a larger range of line ratios owing to (on average) longer exposure times. However, Runco et al. (2021) showed that the differences in the sample are generally small, and indeed when we apply our analysis, as described in Sections 3.3 and 3.5, to individual MOSDEF galaxies (see Appendix B for further detail), we find similar trends to those seen in KBSS galaxies:

scatter is not significantly reduced at non-zero α , and there is no significant anticorrelation between residual metallicity and residual SFR.

Therefore, we conclude that the selection technique does not drive our results and instead the root of the difference likely lies in the different treatment of individual galaxies. Sanders et al. (2018), Topping et al. (2021), and Sanders et al. (2021) bin MOSDEF galaxies by stellar mass rather than treating galaxies individually, potentially allowing for a larger dynamic range in measured oxygen abundance. A full exploration of how binned spectra yield different results to individual galaxies is beyond the scope of this paper, but we can conclude that *individual* KBSS and MOSDEF galaxies are not inconsistent with each other.

4.3. Physical Implications

A redshift invariant FMR is predicted by simulations and analytical models with steady star formation, where the timescales on which the SFR and ISM enrichment fluctuate are comparable (Dayal et al. 2013; Lilly et al. 2013; Torrey et al. 2018). However, significant deviations from the FMR are beginning to emerge, both in high- z observational data (e.g., Curti et al. 2023; Langeroodi & Hjorth 2023; Nakajima et al. 2023) and in hydrodynamical simulations (e.g., Bassini et al. 2024; Garcia et al. 2024a,b).

Contrary to what is predicted by the FMR, simulations find that the strength with which SFR is correlated with MZR scatter changes with redshift. Garcia et al. (2024a) showed that α_{\min} and subsequently the slope of a $\Delta \log(\text{O}/\text{H})$ -SFR relation (Figure 8) evolve with redshift in simulations with relatively smooth SFHs. When star formation is more stochastic (“bursty”), the timescale for SFR fluctuations decreases but the timescale for ISM enrichment remains constant and independent of the SFR, further decoupling SFR and $\Delta \log(\text{O}/\text{H})$ (Torrey et al. 2018). Rapid gas infall can trigger a burst of star formation and may decrease in the star formation efficiency, decoupling the correlation between gas mass and SFR, which is thought to drive the FMR. Using the Feedback in Realistic Environments simulation (FIRE; Hopkins et al. 2018), Bassini et al. (2023) found feedback to be less efficient at high- z , allowing galaxies to retain a high gas fraction, further decoupling SFR and ISM enrichment.

As such, observed high- z deviations from the FMR can be attributed to bursty star formation keeping galaxies from achieving the equilibrium state that generates the local FMR (e.g., Curti et al. 2023; Langeroodi & Hjorth 2023; Nakajima et al. 2023). The trends examined in this paper suggest that such a state of disequilibrium

could persist to $z \sim 2.3$, explaining the deviation of KBSS galaxies from the $z \sim 0$ FMR (Figure 7) and the very weak correlation between residual metallicity and residual SFR (Figures 8 and 9).

FIRE simulations have also suggested that the MZR’s evolution from $z \sim 0 - 3$ is not driven by changes to the gas fraction (observationally probed by SFR), but is instead driven by the enrichment of inflows and outflows, relative to the enrichment of the ISM (Bassini et al. 2024). This suggests that SFR (and by proxy, gas fraction) is not the most fundamental third parameter. The weak correlation between residual metallicity and residual sSFR in KBSS galaxies could be consistent with idea that gas fraction may not be the primary driver of galaxies’ chemical evolution. Alternatively, a lower star formation efficiency due to rapid gas infall, this could also weaken the relationship between SFR and gas fraction, resulting in a weaker correlation between residual metallicity and residual sSFR. At present, we lack the data needed to break the degeneracy between these two cases. Further observations would be needed in order to either measure the metallicity of infalling and outflowing gas or to measure the gas fraction.

5. CONCLUSIONS

We have used both parametric (Section 3.3) and non-parametric (Section 3.5) methods to investigate the relationship between stellar mass, gas-phase oxygen abundance, and SFR and its consistency with the FMR in 273 galaxies from KBSS-MOSFIRE. We use strong-line calibrations to estimate gas-phase oxygen abundance and test eight different calibrations (each of which produces an MZR with a different shape and normalization, see Section 3.2 and Figure 5) to mitigate the potential bias introduced by a single calibration. To account for the effect of subsolar stellar metallicities on the ionizing stellar output, we adopt a metallicity-dependent conversion factor between $\text{H}\alpha$ luminosity and SFR (Section 2.4). For comparison, we also conduct our analysis using SFRs calculated using a locally-calibrated constant conversion factor.

The results of our analysis lead us to conclude that

1. A metallicity-dependent SFR conversion factor results in a lower SFR for more metal-poor galaxies than would be predicted using a constant conversion factor (Figure 3). The associated SFMS may be steeper and offset towards lower SFR (Figure 4). The size of this effect is contingent on the strong-line calibration used to estimate metallicity: calibrations associated with a steeper MZR produce a slightly steeper SFMS (Section 2.4).

2. Across eight strong-line calibrations and two SFR calculations, the parametric method suggests that KBSS galaxies are inconsistent with the FMR (Section 3.3). Adopting a non-zero value of α does not result in a significant reduction in scatter (Figure 6).
3. Across eight strong-line calibrations calculations, KBSS galaxies show weak and marginally significant anticorrelations both between residual metallicity and absolute SFR_{KE12} (top panel, Figure 8) and between residual metallicity and residual $\text{sSFR}_{\text{KE12}}$ (top panel, Figure 9). Adopting $\text{SFR}(Z)$ results in a weaker and less significant anticorrelation (bottom panels of Figures 8 and 9, and Section 3.5), suggesting there may not be a significant $M_{\star}\text{-SFR}(Z)\text{-}Z_g$ correlation in the KBSS sample.
4. Injection-recovery tests based on the demographics of our galaxy sample show that the parametric and non-parametric approaches are only concordant if the anticorrelation between residual metallicity and SFR is significantly stronger than what is observed at $z \sim 2.3$ (Figure 10 and Section 4.1).
5. KBSS galaxies are inconsistent with the locally-defined FMR (Sections 3.4 and 4.2). The significant redshift evolution of the $\Delta \log(\text{O}/\text{H})\text{-SFR}$ anticorrelation (Section 4.2), lack of scatter reduction at any $\alpha \neq 0$ (Figure 6), and offset towards lower gas-phase oxygen abundance at fixed $\mu_{0.32}$ (Figure 7) all point towards an evolving $M_{\star}\text{-}Z_g\text{-SFR}$ relationship.
6. By comparing to results from hydrodynamical simulations, our results suggest that KBSS galaxies may not be in the equilibrium state of the gas regulator model, and that the disequilibrium state that has already been observed at higher redshifts persists to $z \sim 2.3$ (Section 4.3).
7. The weak anticorrelation between residual metallicity and residual sSFR is consistent with two pos-

sible scenarios: rapid gas infall has caused gas fraction and SFR to become less tightly coupled, or gas fraction is not the most fundamental third parameter driving the evolution of the MZR (Section 4.3).

This work highlights the need to be consistent and precise when discussing the FMR as different conclusions can arise depending on the choice of method. Further work is needed in order to understand the nature of the baryon cycle at cosmic noon and why it might differ from the equilibrium conditions that give rise to the FMR. The results presented here are not in tension with alternative explanations of the MZR’s evolution but further work is needed in order to determine whether this is the case and identify other potential third parameters.

ACKNOWLEDGMENTS

This work is based on data obtained at the W. M. Keck Observatory, operated as a scientific partnership among the California Institute of Technology, the University of California, and the National Aeronautics and Space Administration. This work made use of v2.2.1 of the Binary Population and Spectral Synthesis (BPASS) models as described in Eldridge et al. (2017) and Stanway & Eldridge (2018). The Observatory was made possible by the generous financial support of the W. M. Keck Foundation. T.B.M. was supported by a CIERA Fellowship. N.K.C. would like to thank Claude-André Faucher-Giguère and Andrew Marszewski for their insightful comments regarding results from the FIRE simulations, as well as Adam Carnall for his insight on the Bagpipes SED-fitting code. Lastly, the authors wish to recognize and acknowledge the very significant cultural role and reverence that the summit of Maunakea has always had within the Native Hawaiian community. We are most fortunate to have the opportunity to conduct observations from this mountain.

APPENDIX

A. N2 CALIBRATIONS

High- z galaxies are offset from local galaxies in the N2-BPT due to an increase in spectral hardness at fixed gas-phase oxygen abundance (Masters et al. 2014; Steidel et al. 2014; Shapley et al. 2015; Strom et al. 2017; Shapley et al. 2024), showing that changes in N2 are

sensitive to the spectral hardness, not only gas-phase oxygen abundance. O3N2 is sensitive to ionisation parameter (Kewley & Dopita 2002), but in KBSS, O3N2 has been found to be a less biased indicator of oxygen abundance than N2 (Steidel et al. 2014), motivating our preference for O3N2 in the main body of this paper.

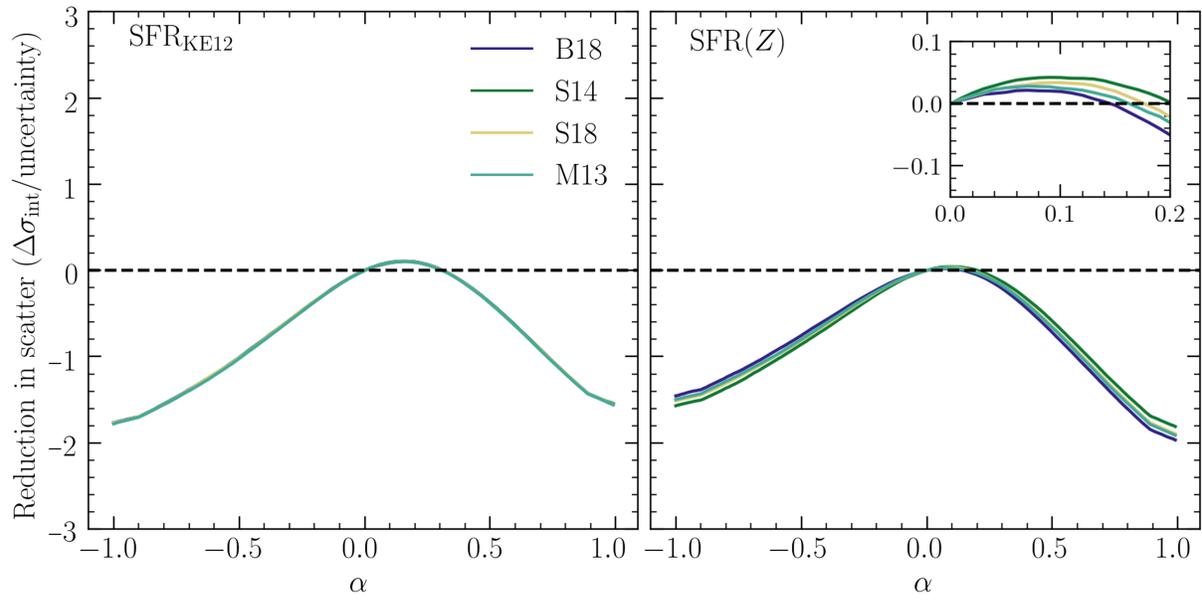


Figure 12. Reduction in scatter vs. α for KBSS galaxies, as in Figure 6, but using N2 calibrations. Each solid curve shows a different calibration, the left-hand panel uses SFR_{KE12} , and the right-hand panel uses $\text{SFR}(Z)$. The inset panel shows the same data as the right-hand panel but limited to $0 \leq \alpha \leq 0.2$ in order to show the effect of adopting $\text{SFR}(Z)$. As was found using O3N2 calibrations, scatter is not significantly reduced at $\alpha \neq 0$.

Table 5. The slope (ψ_1, ψ_2), Spearman’s rank correlation coefficient (ρ_1, ρ_2), p -value (p_1, p_2) for the $\Delta\text{MZR}_{\text{N2}}\text{-SFR}$ and $\Delta\text{MZR}_{\text{N2}}\text{-}\Delta\text{sSFR}$ anticorrelations respectively.

Calibration	SFR	$\Delta \log(\text{O}/\text{H})\text{-SFR}$			$\Delta \log(\text{O}/\text{H})\text{-}\Delta\text{sSFR}$		
		ψ_1	ρ_1	p_1	ψ_2	ρ_2	p_2
M13	KE12	-0.03 ± 0.02	-0.08	0.2	-0.02 ± 0.02	-0.09	0.1
M13	Z	-0.02 ± 0.02	-0.04	0.5	-0.01 ± 0.02	-0.05	0.4
S14	KE12	-0.02 ± 0.01	-0.09	0.2	-0.02 ± 0.01	-0.09	0.1
S14	Z	-0.02 ± 0.01	-0.06	0.4	-0.01 ± 0.01	-0.06	0.3
B18	KE12	-0.03 ± 0.02	-0.08	0.2	-0.03 ± 0.02	-0.09	0.1
B18	Z	-0.03 ± 0.02	-0.03	0.7	-0.009 ± 0.02	-0.04	0.5
S18	KE12	-0.02 ± 0.01	-0.08	0.2	-0.02 ± 0.01	-0.09	0.1
S18	Z	-0.01 ± 0.01	-0.04	0.5	-0.008 ± 0.01	-0.05	0.4

However, N2 requires the observation of just two emission lines with a small wavelength separation, removing the need for multi-band observations. As a result, N2 is frequently used throughout the literature. Hence, while we do not present N2-based results in the main body of the paper, we include them here for completeness.

Figure 12 shows the results of the parametric analysis detailed in Section 3.3. As in Figure 6, we plot reduction in scatter, relative to the MZR scatter, against α . Scatter is not significantly minimized by any $\alpha \neq 0$, suggesting that the N2 sample is inconsistent with the FMR. In fact, the reduction in scatter in the N2 sample is smaller than in the O3N2 sample.

Figures 13 and 14 show the results of the non-parametric analysis detailed in Section 3.5, when adopting the S14 calibration. Across calibrations and SFR estimates, we do not find significant $\Delta \log(\text{O}/\text{H})\text{-SFR}$ and $\Delta \log(\text{O}/\text{H})\text{-}\Delta\text{sSFR}$ (Table 5) anticorrelations. N2-based results can therefore be used to draw the same conclusions as the O3N2 sample: KBSS galaxies are inconsistent with the locally-defined FMR and may show a weak $M_\star\text{-}Z_g\text{-SFR}$ relation.

B. COMPARISON TO MOSDEF

MOSDEF (Kriek et al. 2015) is the most comparable survey to KBSS, targeting the rest-optical spectra of $z \sim 2$ galaxies using the MOSFIRE spectrograph. As a

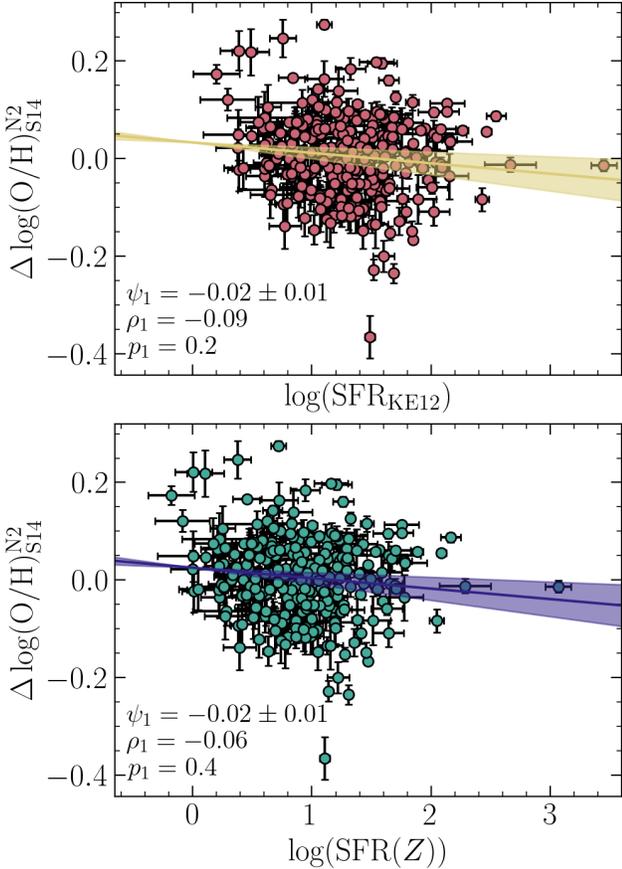


Figure 13. $\Delta \log(\text{O}/\text{H})$ vs. $\log(\text{SFR})$ (top: SFR_{KE12} , bottom: $\text{SFR}(Z)$) for KBSS galaxies, as in Figure 8 but using the S14 N2 calibration. There is no significant anticorrelation between $\Delta \text{MZR}_{\text{N2}}$ and $\log(\text{SFR})$.

result, it is useful to compare the results inferred from these two different surveys. As discussed in Section 4.2, the surveys are based on different selection methods but are generally very similar in terms of stellar mass, dust extinction, and galaxy properties (Runco et al. 2021).

Despite these similarities, our conclusion that KBSS galaxies do not follow the FMR is in tension with reported MOSDEF results (Sanders et al. 2021; Topping et al. 2021). The tension appears to originate in the different treatments of individual galaxy spectra: previous MOSDEF results are reported based on stacked spectra, while we use individual galaxies. Stacked spectra may allow for a larger dynamic range in $\log(\text{O}/\text{H})$, particularly at low metallicity, since stacking allows for weaker emission lines to be measured at a higher signal to noise. However, stacking makes it difficult to measure intrinsic scatter within a galaxy population. Due to the difference in observing strategies, individual KBSS spectra span a larger dynamic range in line ratios than individual MOSDEF spectra. As a result, using individual

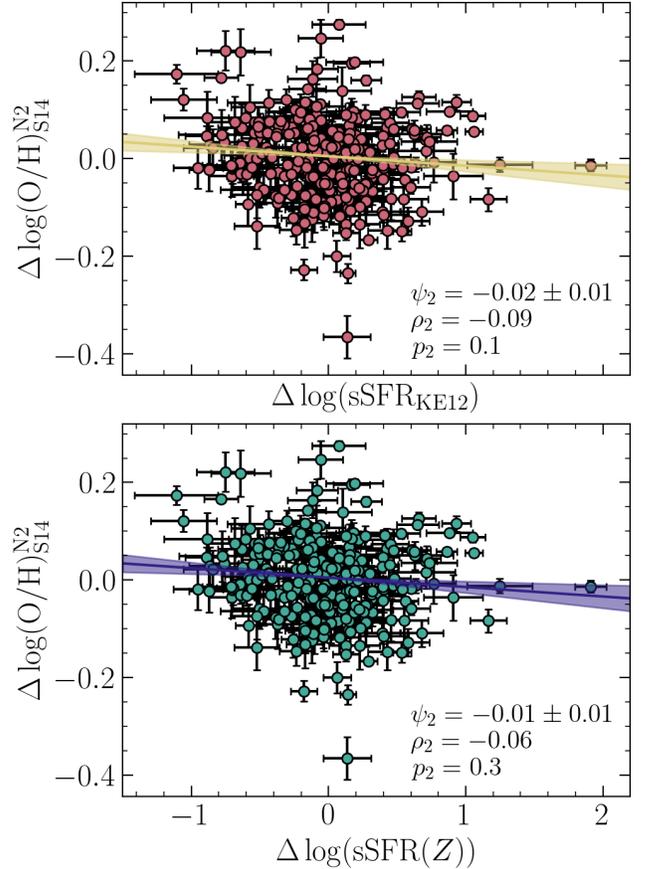


Figure 14. $\Delta \log(\text{O}/\text{H})$ vs. $\Delta(\text{sSFR})$ (top: SFR_{KE12} , bottom: $\text{SFR}(Z)$) for KBSS galaxies, as in Figure 9 but using the S14 N2 calibration. There is no significant anticorrelation between $\Delta \text{MZR}_{\text{N2}}$ and $\Delta \log(\text{sSFR})$.

galaxies instead of stacks may more drastically curtail the dynamic range of $\log(\text{O}/\text{H})$ in MOSDEF than in KBSS, potentially explaining why MOSDEF results are significantly different when individual galaxies are analyzed. Here, we show that when we apply the analysis outlined in Sections 3.3 and 3.5 to individual MOSDEF galaxies, the results are in fact aligned.

Using the line measurements made public by the MOSDEF team, we impose the same SNR cuts ($\text{SNR} > 3$ for $\text{H}\alpha$, $\text{H}\beta$, $[\text{O III}]\lambda 5007$, and $[\text{N II}]\lambda 6885$, and $\text{SNR} > 5$ for $\text{H}\alpha/\text{H}\beta$). We take the stellar masses from the 3D-HST catalog (Skelton et al. 2014), which also assume a Chabrier (2003) IMF, and make a further cut to exclude galaxies with $\log(M_*/M_\odot) < 9$ as the sample is incomplete below this mass (Topping et al. 2021). To ensure we construct a comparable sample to the KBSS sample presented in this paper, we also restrict the sample to galaxies in the redshift range $1.90 \leq z \leq 2.61$. After making these cuts, we obtained a sample of 233 galaxies with well-measured O3N2 and 260 galaxies with well-

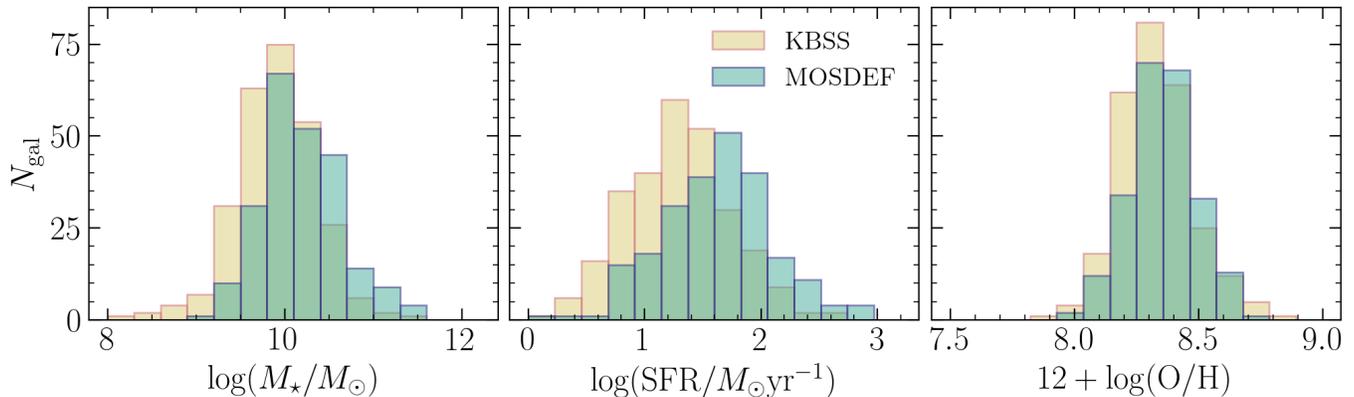


Figure 15. Histograms showing the distribution of (left to right) stellar mass, SFR, and oxygen abundance in KBSS (yellow) and MOSDEF (teal). MOSDEF includes more high-mass, more highly star forming galaxies than KBSS, although the distribution of $12 + \log(\text{O}/\text{H})$ is comparable between the two samples. The M_* - Z_g -SFR correlation may be stronger for higher mass galaxies.

measured N2. The distribution in stellar mass, SFR, and oxygen abundance in the O3N2 sample can be seen in Figure 15. Since no characteristic uncertainty is reported for these stellar masses, we adopt a conservative estimate of 0.1 dex as the uncertainty on stellar mass, equal to the median uncertainty for KBSS stellar masses. In reality, we recognize that the true uncertainty is likely lower, due to the more extensive photometry available for the stellar mass estimates. SFR is estimated from the H α luminosity, using both the KE12 conversion factor and a metallicity-dependent conversion factor.

Runco et al. (2021) found the spectroscopic KBSS and MOSDEF samples to be comparable, with some slight differences in the median stellar mass. Once our quality cuts are made, this difference becomes more pronounced, and we also see a significant difference in the median SFR (see Figure 15). Compared to the KBSS O3N2 sample, the MOSDEF O3N2 sample has a higher median stellar mass ($1.35 \times 10^{10} M_\odot$, 0.3 dex larger than the median mass in the KBSS) and a higher SFR ($44 M_\odot \text{yr}^{-1}$, 0.15 dex higher than in KBSS). However, a full exploration of the effect of sample differences on the nature of the M_* - Z_g -SFR relationship is beyond the scope of this paper.

First, we apply the parametric method, which measures the scatter in the correlation between $12 + \log(\text{O}/\text{H})$ and μ_α . See Section 3.3 for further detail regarding the parametric method. Figure 16 shows the reduction in scatter at different values of α . When using SFR_{KE12} (cf. left panel of Figure 16), scatter is minimised by 1.5σ at $\alpha \sim 0.5$. This level of reduction is larger than in KBSS (left panel of Figure 6), although still only marginally significant. As is seen in KBSS (right panel of Figure 6) and explained in Section 3.5,

adopting $\text{SFR}(Z)$ suppresses the reduction in scatter. Strong-line calibrations with a larger $|B|$ factor (see Table 1) are associated with a stronger suppression of the reduction in scatter. In the case of PP04 and B18, scatter is reduced by $< 1\sigma$, and in the case of M13 and S18, the reduction in scatter remains marginal at $< 1.5\sigma$. Thus, while MOSDEF galaxies do show a more significant reduction in scatter than KBSS galaxies, the results remain consistent and we cannot confidently conclude that MOSDEF galaxies show a significant reduction in scatter when incorporating SFR as a third parameter.

Next, we use the non-parametric method (Section 3.5) to quantify any $\Delta \log(\text{O}/\text{H})$ -SFR and $\Delta \log(\text{O}/\text{H})$ - ΔsSFR correlations. More significant differences between MOSDEF and KBSS emerge here. Across strong-line calibrations (both O3N2- and N2-based) and SFR calculations, we measure significant $\Delta \log(\text{O}/\text{H})$ -SFR and $\Delta \log(\text{O}/\text{H})$ - ΔsSFR anticorrelations. Given the larger reduction in scatter seen in MOSDEF (Figure 16) and the analysis presented in Section 4.1, this is unsurprising. MOSDEF galaxies are associated with steeper $\Delta \log(\text{O}/\text{H})$ -SFR (Figure 17) and $\Delta \log(\text{O}/\text{H})$ - ΔsSFR (Figure 18) slopes, more negative Spearman- ρ values, and a higher statistical significance. Moreover, we recover a similar $\Delta \log(\text{O}/\text{H})$ - ΔsSFR slope to Sanders et al. (2018), who found a slope of -0.14 ± 0.034 for $z \sim 2.3$ MOSDEF galaxies.

Notably, the $\Delta \log(\text{O}/\text{H})$ - ΔsSFR slope is much shallower than the slope associated with $z \sim 0$ SDSS stacks, as is discussed in Section 4.2, this implies that MOSDEF galaxies are also inconsistent with a redshift-invariant FMR. The fact that MOSDEF galaxies in our sample and SDSS galaxies generally have higher stellar masses and SFRs than KBSS galaxies may suggest that M_* - Z_g -SFR correlations are stronger in higher mass galaxies.

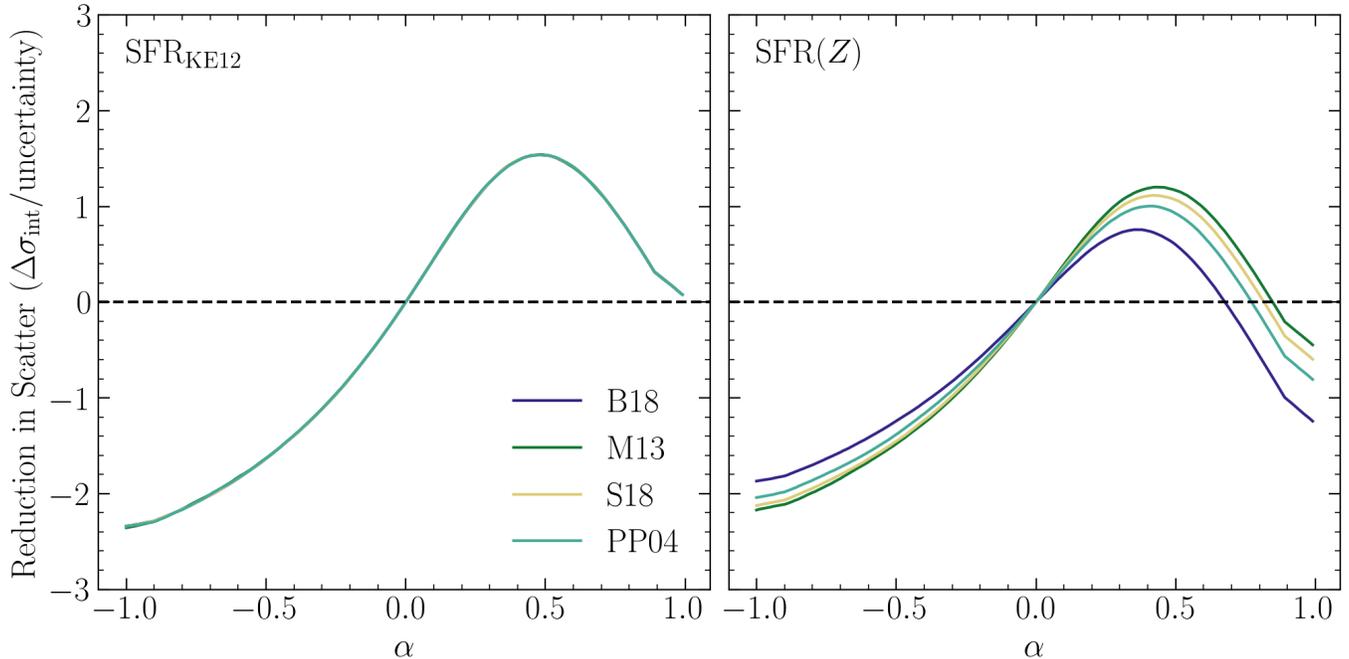


Figure 16. Reduction in scatter vs. α , as in Figures 6 and 12, but for MOSDEF galaxies, using SFR_{KE12} (left) and $\text{SFR}(Z)$ (right). Each solid curve shows a different O3N2 calibration. As in the KBSS sample, scatter is not significantly reduced by any value of α , and scatter reduction is suppressed by adopting $\text{SFR}(Z)$.

REFERENCES

- Adelberger, K. L., Steidel, C. C., Shapley, A. E., et al. 2004, *ApJ*, 607, 226, doi: [10.1086/383221](https://doi.org/10.1086/383221)
- Andrews, B. H., & Martini, P. 2013, *ApJ*, 765, 140, doi: [10.1088/0004-637X/765/2/140](https://doi.org/10.1088/0004-637X/765/2/140)
- Asplund, M., Grevesse, N., Sauval, A. J., & Scott, P. 2009, *ARA&A*, 47, 481, doi: [10.1146/annurev.astro.46.060407.145222](https://doi.org/10.1146/annurev.astro.46.060407.145222)
- Bassini, L., Feldmann, R., Gensior, J., et al. 2024, *MNRAS*, 532, L14, doi: [10.1093/mnras/slae036](https://doi.org/10.1093/mnras/slae036)
- . 2023, *MNRAS*, 525, 5388, doi: [10.1093/mnras/stad2617](https://doi.org/10.1093/mnras/stad2617)
- Bian, F., Kewley, L. J., & Dopita, M. A. 2018, *ApJ*, 859, 175, doi: [10.3847/1538-4357/aabd74](https://doi.org/10.3847/1538-4357/aabd74)
- Bothwell, M. S., Maiolino, R., Peng, Y., et al. 2016, *MNRAS*, 455, 1156, doi: [10.1093/mnras/stv2121](https://doi.org/10.1093/mnras/stv2121)
- Bruzual, G., & Charlot, S. 2003, *MNRAS*, 344, 1000, doi: [10.1046/j.1365-8711.2003.06897.x](https://doi.org/10.1046/j.1365-8711.2003.06897.x)
- Calabrò, A., Amorín, R., Fontana, A., et al. 2017, *A&A*, 601, A95, doi: [10.1051/0004-6361/201629762](https://doi.org/10.1051/0004-6361/201629762)
- Cardelli, J. A., Clayton, G. C., & Mathis, J. S. 1989, *ApJ*, 345, 245, doi: [10.1086/167900](https://doi.org/10.1086/167900)
- Carnall, A. C., Leja, J., Johnson, B. D., et al. 2019, *ApJ*, 873, 44, doi: [10.3847/1538-4357/ab04a2](https://doi.org/10.3847/1538-4357/ab04a2)
- Carnall, A. C., McLure, R. J., Dunlop, J. S., & Davé, R. 2018, *MNRAS*, 480, 4379, doi: [10.1093/mnras/sty2169](https://doi.org/10.1093/mnras/sty2169)
- Chabrier, G. 2003, *PASP*, 115, 763, doi: [10.1086/376392](https://doi.org/10.1086/376392)
- Cowie, L. L., & Barger, A. J. 2008, *ApJ*, 686, 72, doi: [10.1086/591176](https://doi.org/10.1086/591176)
- Cresci, G., Mannucci, F., Sommariva, V., et al. 2012, *MNRAS*, 421, 262, doi: [10.1111/j.1365-2966.2011.20299.x](https://doi.org/10.1111/j.1365-2966.2011.20299.x)
- Cullen, F., McLure, R. J., Dunlop, J. S., et al. 2019, *MNRAS*, 487, 2038, doi: [10.1093/mnras/stz1402](https://doi.org/10.1093/mnras/stz1402)
- Curti, M., Mannucci, F., Cresci, G., & Maiolino, R. 2020, *MNRAS*, 491, 944, doi: [10.1093/mnras/stz2910](https://doi.org/10.1093/mnras/stz2910)
- Curti, M., D'Eugenio, F., Carniani, S., et al. 2023, *MNRAS*, 518, 425, doi: [10.1093/mnras/stac2737](https://doi.org/10.1093/mnras/stac2737)
- Curti, M., Maiolino, R., Curtis-Lake, E., et al. 2024, *A&A*, 684, A75, doi: [10.1051/0004-6361/202346698](https://doi.org/10.1051/0004-6361/202346698)
- Davé, R., Rafieferantsoa, M. H., Thompson, R. J., & Hopkins, P. F. 2017, *MNRAS*, 467, 115, doi: [10.1093/mnras/stx108](https://doi.org/10.1093/mnras/stx108)
- Dayal, P., Ferrara, A., & Dunlop, J. S. 2013, *MNRAS*, 430, 2891, doi: [10.1093/mnras/stt083](https://doi.org/10.1093/mnras/stt083)
- Donnari, M., Pillepich, A., Nelson, D., et al. 2019, *MNRAS*, 485, 4817, doi: [10.1093/mnras/stz712](https://doi.org/10.1093/mnras/stz712)
- Eldridge, J. J., Stanway, E. R., Xiao, L., et al. 2017, *PASA*, 34, e058, doi: [10.1017/pasa.2017.51](https://doi.org/10.1017/pasa.2017.51)
- Ellison, S. L., Patton, D. R., Simard, L., & McConnachie, A. W. 2008, *ApJL*, 672, L107, doi: [10.1086/527296](https://doi.org/10.1086/527296)

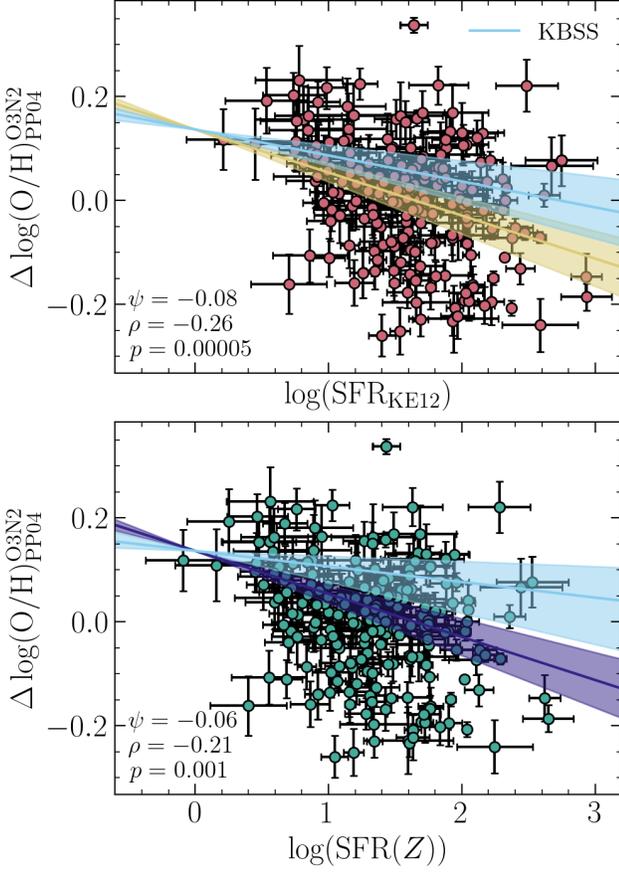


Figure 17. $\Delta \log(\text{O}/\text{H})$ vs. $\log(\text{SFR}_{\text{KE12}})$, as in Figures 8 and 13, but using MOSDEF galaxies. The top panel uses SFR_{KE12} and the bottom panel uses $\text{SFR}(Z)$. The slopes found for KBSS (Figure 8) are shown in light blue. The anticorrelation is stronger and more significant than what is found for KBSS but still shallower than what is found for local galaxies, implying a redshift evolution.

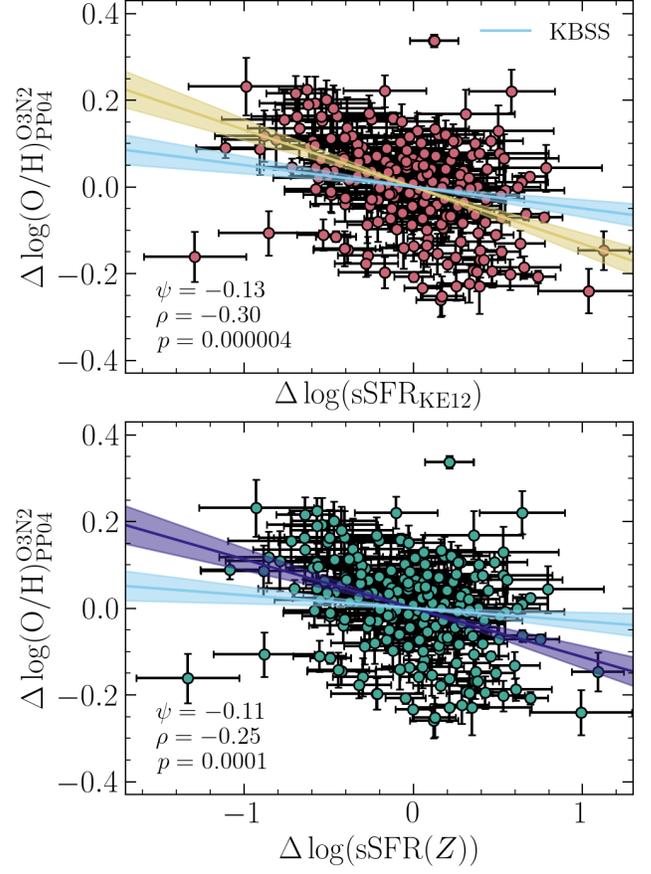


Figure 18. $\Delta \log(\text{O}/\text{H})$ vs. $\Delta \log(\text{sSFR}_{\text{KE12}})$, as in Figures 9 and 14, but using MOSDEF galaxies. The top panel uses SFR_{KE12} and the bottom panel uses $\text{SFR}(Z)$. For comparison, the KBSS regression line (Figure 9) is shown in light blue. As in Figure 17, the anticorrelation is stronger and more significant than in KBSS and weaker than in local galaxies, implying a redshift evolution.

Erb, D. K., Shapley, A. E., Pettini, M., et al. 2006, *ApJ*, 644, 813, doi: [10.1086/503623](https://doi.org/10.1086/503623)

Ferland, G. J., Chatzikos, M., Guzmán, F., et al. 2017, *RMxAA*, 53, 385, doi: [10.48550/arXiv.1705.10877](https://doi.org/10.48550/arXiv.1705.10877)

Finlator, K., & Davé, R. 2008, *MNRAS*, 385, 2181, doi: [10.1111/j.1365-2966.2008.12991.x](https://doi.org/10.1111/j.1365-2966.2008.12991.x)

Garcia, A. M., Torrey, P., Ellison, S., et al. 2024a, *MNRAS*, 531, 1398, doi: [10.1093/mnras/stae1252](https://doi.org/10.1093/mnras/stae1252)

Garcia, A. M., Torrey, P., Ellison, S. L., et al. 2024b, *MNRAS*, doi: [10.1093/mnras/stae2587](https://doi.org/10.1093/mnras/stae2587)

Garnett, D. R. 2002, *ApJ*, 581, 1019, doi: [10.1086/344301](https://doi.org/10.1086/344301)

Gordon, K. D., Clayton, G. C., Misselt, K. A., Landolt, A. U., & Wolff, M. J. 2003, *ApJ*, 594, 279, doi: [10.1086/376774](https://doi.org/10.1086/376774)

Hopkins, P. F., Wetzell, A., Kereš, D., et al. 2018, *MNRAS*, 480, 800, doi: [10.1093/mnras/sty1690](https://doi.org/10.1093/mnras/sty1690)

Hsiao, T. Y.-Y., Álvarez-Márquez, J., Coe, D., et al. 2024, *arXiv e-prints*, arXiv:2404.16200, doi: [10.48550/arXiv.2404.16200](https://doi.org/10.48550/arXiv.2404.16200)

Kacprzak, G. G., van de Voort, F., Glazebrook, K., et al. 2016, *ApJL*, 826, L11, doi: [10.3847/2041-8205/826/1/L11](https://doi.org/10.3847/2041-8205/826/1/L11)

Kashino, D., Silverman, J. D., Sanders, D., et al. 2017, *ApJ*, 835, 88, doi: [10.3847/1538-4357/835/1/88](https://doi.org/10.3847/1538-4357/835/1/88)

Kelly, B. C. 2007, *ApJ*, 665, 1489, doi: [10.1086/519947](https://doi.org/10.1086/519947)

Kennicutt, R. C., & Evans, N. J. 2012, *ARA&A*, 50, 531, doi: [10.1146/annurev-astro-081811-125610](https://doi.org/10.1146/annurev-astro-081811-125610)

Kewley, L. J., & Dopita, M. A. 2002, *ApJS*, 142, 35, doi: [10.1086/341326](https://doi.org/10.1086/341326)

Kobayashi, C., Karakas, A. I., & Lugaro, M. 2020, *ApJ*, 900, 179, doi: [10.3847/1538-4357/abae65](https://doi.org/10.3847/1538-4357/abae65)

Kobayashi, C., Springel, V., & White, S. D. M. 2007, *MNRAS*, 376, 1465, doi: [10.1111/j.1365-2966.2007.11555.x](https://doi.org/10.1111/j.1365-2966.2007.11555.x)

- Kriek, M., Shapley, A. E., Reddy, N. A., et al. 2015, *ApJS*, 218, 15, doi: [10.1088/0067-0049/218/2/15](https://doi.org/10.1088/0067-0049/218/2/15)
- Kroupa, P. 2001, *MNRAS*, 322, 231, doi: [10.1046/j.1365-8711.2001.04022.x](https://doi.org/10.1046/j.1365-8711.2001.04022.x)
- Langeroodi, D., & Hjorth, J. 2023, arXiv e-prints, arXiv:2307.06336, doi: [10.48550/arXiv.2307.06336](https://doi.org/10.48550/arXiv.2307.06336)
- Lara-López, M. A., Cepa, J., Bongiovanni, A., et al. 2010, *A&A*, 521, L53, doi: [10.1051/0004-6361/201014803](https://doi.org/10.1051/0004-6361/201014803)
- Laseter, I. H., Maseda, M. V., Curti, M., et al. 2024, *A&A*, 681, A70, doi: [10.1051/0004-6361/202347133](https://doi.org/10.1051/0004-6361/202347133)
- Leitherer, C., & Heckman, T. M. 1995, *ApJS*, 96, 9, doi: [10.1086/192112](https://doi.org/10.1086/192112)
- Leja, J., Carnall, A. C., Johnson, B. D., Conroy, C., & Speagle, J. S. 2019, *ApJ*, 876, 3, doi: [10.3847/1538-4357/ab133c](https://doi.org/10.3847/1538-4357/ab133c)
- Leja, J., Speagle, J. S., Ting, Y.-S., et al. 2022, *ApJ*, 936, 165, doi: [10.3847/1538-4357/ac887d](https://doi.org/10.3847/1538-4357/ac887d)
- Lequeux, J., Peimbert, M., Rayo, J. F., Serrano, A., & Torres-Peimbert, S. 1979, *A&A*, 80, 155
- Lilly, S. J., Carollo, C. M., Pipino, A., Renzini, A., & Peng, Y. 2013, *ApJ*, 772, 119, doi: [10.1088/0004-637X/772/2/119](https://doi.org/10.1088/0004-637X/772/2/119)
- Liu, X., Shapley, A. E., Coil, A. L., Brinchmann, J., & Ma, C.-P. 2008, *ApJ*, 678, 758, doi: [10.1086/529030](https://doi.org/10.1086/529030)
- Maier, C., Lilly, S. J., Ziegler, B. L., et al. 2014, *ApJ*, 792, 3, doi: [10.1088/0004-637X/792/1/3](https://doi.org/10.1088/0004-637X/792/1/3)
- Maier, C., Ziegler, B. L., Lilly, S. J., et al. 2015, *A&A*, 577, A14, doi: [10.1051/0004-6361/201425224](https://doi.org/10.1051/0004-6361/201425224)
- Maiolino, R., Nagao, T., Grazian, A., et al. 2008, *A&A*, 488, 463, doi: [10.1051/0004-6361:200809678](https://doi.org/10.1051/0004-6361:200809678)
- Mannucci, F., Cresci, G., Maiolino, R., Marconi, A., & Gnerucci, A. 2010, *MNRAS*, 408, 2115, doi: [10.1111/j.1365-2966.2010.17291.x](https://doi.org/10.1111/j.1365-2966.2010.17291.x)
- Mannucci, F., Cresci, G., Maiolino, R., et al. 2009, *MNRAS*, 398, 1915, doi: [10.1111/j.1365-2966.2009.15185.x](https://doi.org/10.1111/j.1365-2966.2009.15185.x)
- Marino, R. A., Rosales-Ortega, F. F., Sánchez, S. F., et al. 2013, *A&A*, 559, A114, doi: [10.1051/0004-6361/201321956](https://doi.org/10.1051/0004-6361/201321956)
- Masters, D., McCarthy, P., Siana, B., et al. 2014, *ApJ*, 785, 153, doi: [10.1088/0004-637X/785/2/153](https://doi.org/10.1088/0004-637X/785/2/153)
- McAlpine, S., Helly, J. C., Schaller, M., et al. 2016, *Astronomy and Computing*, 15, 72, doi: [10.1016/j.ascom.2016.02.004](https://doi.org/10.1016/j.ascom.2016.02.004)
- McGaugh, S. S. 1991, *ApJ*, 380, 140, doi: [10.1086/170569](https://doi.org/10.1086/170569)
- McLean, I. S., Steidel, C. C., Epps, H. W., et al. 2012, in *Society of Photo-Optical Instrumentation Engineers (SPIE) Conference Series*, Vol. 8446, *Ground-based and Airborne Instrumentation for Astronomy IV*, ed. I. S. McLean, S. K. Ramsay, & H. Takami, 84460J, doi: [10.1117/12.924794](https://doi.org/10.1117/12.924794)
- Nakajima, K., Ouchi, M., Isobe, Y., et al. 2023, *ApJS*, 269, 33, doi: [10.3847/1538-4365/acd556](https://doi.org/10.3847/1538-4365/acd556)
- Nelson, D., Pillepich, A., Springel, V., et al. 2019, *MNRAS*, 490, 3234, doi: [10.1093/mnras/stz2306](https://doi.org/10.1093/mnras/stz2306)
- Oke, J. B., Cohen, J. G., Carr, M., et al. 1995, *PASP*, 107, 375, doi: [10.1086/133562](https://doi.org/10.1086/133562)
- Onodera, M., Carollo, C. M., Lilly, S., et al. 2016, *ApJ*, 822, 42, doi: [10.3847/0004-637X/822/1/42](https://doi.org/10.3847/0004-637X/822/1/42)
- Osterbrock, D. E. 1989, *Astrophysics of gaseous nebulae and active galactic nuclei*
- Panter, B., Jimenez, R., Heavens, A. F., & Charlot, S. 2008, *MNRAS*, 391, 1117, doi: [10.1111/j.1365-2966.2008.13981.x](https://doi.org/10.1111/j.1365-2966.2008.13981.x)
- Pérez-Montero, E., Contini, T., Lamareille, F., et al. 2009, *A&A*, 495, 73, doi: [10.1051/0004-6361:200810558](https://doi.org/10.1051/0004-6361:200810558)
- Pettini, M., & Pagel, B. E. J. 2004, *MNRAS*, 348, L59, doi: [10.1111/j.1365-2966.2004.07591.x](https://doi.org/10.1111/j.1365-2966.2004.07591.x)
- Pilyugin, L. S., Vílchez, J. M., & Contini, T. 2004, *A&A*, 425, 849, doi: [10.1051/0004-6361:20034522](https://doi.org/10.1051/0004-6361:20034522)
- Pilyugin, L. S., Vílchez, J. M., & Thuan, T. X. 2010, *ApJ*, 720, 1738, doi: [10.1088/0004-637X/720/2/1738](https://doi.org/10.1088/0004-637X/720/2/1738)
- Reddy, N. A., Pettini, M., Steidel, C. C., et al. 2012, *ApJ*, 754, 25, doi: [10.1088/0004-637X/754/1/25](https://doi.org/10.1088/0004-637X/754/1/25)
- Revalski, M., Rafelski, M., Henry, A., et al. 2024, *ApJ*, 966, 228, doi: [10.3847/1538-4357/ad382c](https://doi.org/10.3847/1538-4357/ad382c)
- Rogers, N. S. J., Strom, A. L., Rudie, G. C., et al. 2024, *ApJL*, 964, L12, doi: [10.3847/2041-8213/ad2f37](https://doi.org/10.3847/2041-8213/ad2f37)
- Rudie, G. C., Steidel, C. C., Trainor, R. F., et al. 2012, *ApJ*, 750, 67, doi: [10.1088/0004-637X/750/1/67](https://doi.org/10.1088/0004-637X/750/1/67)
- Runco, J. N., Shapley, A. E., Sanders, R. L., et al. 2021, *MNRAS*, 502, 2600, doi: [10.1093/mnras/stab119](https://doi.org/10.1093/mnras/stab119)
- Salim, S., Lee, J. C., Davé, R., & Dickinson, M. 2015, *ApJ*, 808, 25, doi: [10.1088/0004-637X/808/1/25](https://doi.org/10.1088/0004-637X/808/1/25)
- Salim, S., Lee, J. C., Ly, C., et al. 2014, *ApJ*, 797, 126, doi: [10.1088/0004-637X/797/2/126](https://doi.org/10.1088/0004-637X/797/2/126)
- Sánchez, S. F., Rosales-Ortega, F. F., Marino, R. A., et al. 2012, *A&A*, 546, A2, doi: [10.1051/0004-6361/201219578](https://doi.org/10.1051/0004-6361/201219578)
- Sánchez, S. F., Rosales-Ortega, F. F., Jungwiert, B., et al. 2013, *A&A*, 554, A58, doi: [10.1051/0004-6361/201220669](https://doi.org/10.1051/0004-6361/201220669)
- Sanders, R. L., Shapley, A. E., Topping, M. W., Reddy, N. A., & Brammer, G. B. 2024, *ApJ*, 962, 24, doi: [10.3847/1538-4357/ad15fc](https://doi.org/10.3847/1538-4357/ad15fc)
- Sanders, R. L., Shapley, A. E., Kriek, M., et al. 2015, *ApJ*, 799, 138, doi: [10.1088/0004-637X/799/2/138](https://doi.org/10.1088/0004-637X/799/2/138)
- . 2018, *ApJ*, 858, 99, doi: [10.3847/1538-4357/aabcbcd](https://doi.org/10.3847/1538-4357/aabcbcd)
- Sanders, R. L., Shapley, A. E., Reddy, N. A., et al. 2020, *MNRAS*, 491, 1427, doi: [10.1093/mnras/stz3032](https://doi.org/10.1093/mnras/stz3032)
- Sanders, R. L., Shapley, A. E., Jones, T., et al. 2021, *ApJ*, 914, 19, doi: [10.3847/1538-4357/abf4c1](https://doi.org/10.3847/1538-4357/abf4c1)

- Savaglio, S., Glazebrook, K., Le Borgne, D., et al. 2005, *ApJ*, 635, 260, doi: [10.1086/497331](https://doi.org/10.1086/497331)
- Schaerer, D., Marques-Chaves, R., Barrufet, L., et al. 2022, *A&A*, 665, L4, doi: [10.1051/0004-6361/202244556](https://doi.org/10.1051/0004-6361/202244556)
- Scholte, D., Cullen, F., Carnall, A. C., et al. 2025, arXiv e-prints, arXiv:2502.10499, doi: [10.48550/arXiv.2502.10499](https://doi.org/10.48550/arXiv.2502.10499)
- Shapley, A. E., Sanders, R. L., Reddy, N. A., Topping, M. W., & Brammer, G. B. 2023, *ApJ*, 954, 157, doi: [10.3847/1538-4357/acea5a](https://doi.org/10.3847/1538-4357/acea5a)
- Shapley, A. E., Reddy, N. A., Kriek, M., et al. 2015, *ApJ*, 801, 88, doi: [10.1088/0004-637X/801/2/88](https://doi.org/10.1088/0004-637X/801/2/88)
- Shapley, A. E., Sanders, R. L., Topping, M. W., et al. 2024, arXiv e-prints, arXiv:2407.00157, doi: [10.48550/arXiv.2407.00157](https://doi.org/10.48550/arXiv.2407.00157)
- Skelton, R. E., Whitaker, K. E., Momcheva, I. G., et al. 2014, *ApJS*, 214, 24, doi: [10.1088/0067-0049/214/2/24](https://doi.org/10.1088/0067-0049/214/2/24)
- Stanton, T. M., Cullen, F., McLure, R. J., et al. 2024, *MNRAS*, 532, 3102, doi: [10.1093/mnras/stae1705](https://doi.org/10.1093/mnras/stae1705)
- Stanway, E. R., & Eldridge, J. J. 2018, *MNRAS*, 479, 75, doi: [10.1093/mnras/sty1353](https://doi.org/10.1093/mnras/sty1353)
- Steidel, C. C., Shapley, A. E., Pettini, M., et al. 2004, *ApJ*, 604, 534, doi: [10.1086/381960](https://doi.org/10.1086/381960)
- Steidel, C. C., Strom, A. L., Pettini, M., et al. 2016, *ApJ*, 826, 159, doi: [10.3847/0004-637X/826/2/159](https://doi.org/10.3847/0004-637X/826/2/159)
- Steidel, C. C., Rudie, G. C., Strom, A. L., et al. 2014, *ApJ*, 795, 165, doi: [10.1088/0004-637X/795/2/165](https://doi.org/10.1088/0004-637X/795/2/165)
- Storey, P. J., & Zeppen, C. J. 2000, *MNRAS*, 312, 813, doi: [10.1046/j.1365-8711.2000.03184.x](https://doi.org/10.1046/j.1365-8711.2000.03184.x)
- Strom, A. L., Rudie, G. C., Steidel, C. C., & Trainor, R. F. 2022, *ApJ*, 925, 116, doi: [10.3847/1538-4357/ac38a3](https://doi.org/10.3847/1538-4357/ac38a3)
- Strom, A. L., Steidel, C. C., Rudie, G. C., Trainor, R. F., & Pettini, M. 2018, *ApJ*, 868, 117, doi: [10.3847/1538-4357/aae1a5](https://doi.org/10.3847/1538-4357/aae1a5)
- Strom, A. L., Steidel, C. C., Rudie, G. C., et al. 2017, *ApJ*, 836, 164, doi: [10.3847/1538-4357/836/2/164](https://doi.org/10.3847/1538-4357/836/2/164)
- Theios, R. L., Steidel, C. C., Strom, A. L., et al. 2019, *ApJ*, 871, 128, doi: [10.3847/1538-4357/aaf386](https://doi.org/10.3847/1538-4357/aaf386)
- Topping, M. W., Shapley, A. E., Reddy, N. A., et al. 2020, *MNRAS*, 499, 1652, doi: [10.1093/mnras/staa2941](https://doi.org/10.1093/mnras/staa2941)
- Topping, M. W., Shapley, A. E., Sanders, R. L., et al. 2021, *MNRAS*, 506, 1237, doi: [10.1093/mnras/stab1793](https://doi.org/10.1093/mnras/stab1793)
- Torrey, P., Vogelsberger, M., Genel, S., et al. 2014, *MNRAS*, 438, 1985, doi: [10.1093/mnras/stt2295](https://doi.org/10.1093/mnras/stt2295)
- Torrey, P., Vogelsberger, M., Hernquist, L., et al. 2018, *MNRAS*, 477, L16, doi: [10.1093/mnrasl/sly031](https://doi.org/10.1093/mnrasl/sly031)
- Tremonti, C. A., Heckman, T. M., Kauffmann, G., et al. 2004, *ApJ*, 613, 898, doi: [10.1086/423264](https://doi.org/10.1086/423264)
- Troncoso, P., Maiolino, R., Sommariva, V., et al. 2014, *A&A*, 563, A58, doi: [10.1051/0004-6361/201322099](https://doi.org/10.1051/0004-6361/201322099)
- Whitaker, K. E., Franx, M., Leja, J., et al. 2014, *ApJ*, 795, 104, doi: [10.1088/0004-637X/795/2/104](https://doi.org/10.1088/0004-637X/795/2/104)
- Wuyts, E., Wisnioski, E., Fossati, M., et al. 2016, *ApJ*, 827, 74, doi: [10.3847/0004-637X/827/1/74](https://doi.org/10.3847/0004-637X/827/1/74)
- Yabe, K., Ohta, K., Akiyama, M., et al. 2015, *PASJ*, 67, 102, doi: [10.1093/pasj/psv079](https://doi.org/10.1093/pasj/psv079)
- Yates, R. M., Kauffmann, G., & Guo, Q. 2012, *MNRAS*, 422, 215, doi: [10.1111/j.1365-2966.2012.20595.x](https://doi.org/10.1111/j.1365-2966.2012.20595.x)
- York, D. G., Adelman, J., Anderson, John E., J., et al. 2000, *AJ*, 120, 1579, doi: [10.1086/301513](https://doi.org/10.1086/301513)
- Zahid, H. J., Kashino, D., Silverman, J. D., et al. 2014, *ApJ*, 792, 75, doi: [10.1088/0004-637X/792/1/75](https://doi.org/10.1088/0004-637X/792/1/75)
- Zhang, F., Li, L., Kang, X., Zhuang, Y., & Han, Z. 2013, *MNRAS*, 433, 1039, doi: [10.1093/mnras/stt785](https://doi.org/10.1093/mnras/stt785)